Article

Not peer-reviewed version

X- and Ku-Band Sar Backscattering Signatures of Snow-Covered Lake Ice and Sea Ice

Katriina Veijola [*], Juval Cohen, Marko Mäkynen, Juha Lemmetyinen, Jaan Praks, Bin Cheng

Posted Date: 6 November 2023

doi: 10.20944/preprints202311.0286.v1

Keywords: remote sensing; synthetic aperture radar; sea ice; snow doi:10.20944/preprints202311.0286.v1

Article

X- and Ku-band SAR Backscattering Signatures of Snow-Covered Lake Ice And Sea Ice

Katriina Veijola [1],*, Juval Cohen [1], Marko Mäkynen [1], Juha Lemmetyinen [1], Jaan Praks [2] and Bin Cheng [1]

[1] Finnish Meteorological Institute, P.O.Box 503, FI-00101 Helsinki, Finland
[2] Aalto University, Department of Electronics and Nanoengineering, P.O.Box 15500, FI-00076 AALTO, Finland
* Correspondence: Katriina.Veijola@ fmi.fi; Tel.: +358-50-910-8270

Abstract: In this work, backscattering signatures of snow-covered lake ice and sea ice from X- and Ku-band synthetic aperture radar (SAR) data are investigated. The SAR data were acquired with the ESA airborne SnowSAR sensor in winter 2012 over Lake Orajärvi in northern Finland and over landfast ice in the Bay of Bothnia of the Baltic Sea. Co-incident with the SnowSAR acquisitions in-situ snow and ice data were measured. In addition, time series of TerraSAR-X images and ice mass balance buoy data were acquired for the Lake Orajärvi in 2011-12. The main objective of our study was to investigate relationships between SAR backscattering signatures and snow depth over lake and sea ice, with the ultimate objective of assessing the feasibility of retrieval of snow characteristics using X- and Ku-band dual-polarisation (VV and VH) SAR over freshwater or sea ice. This study constitutes the first comprehensive survey of snow backscattering signatures at these two combined frequencies over both lake and sea ice. For lake ice, we show that X-band VH-polarized backscattering coefficient (σ^o) and the Ku-band VV/VH-ratio exhibited the highest sensitivity to the snow depth. For sea ice, the highest sensitivity to the snow depth was found from the Ku-band VV-polarised σ^o and the Ku-band VV/VH-ratio. However, the observed relations were relatively weak, indicating that at least for the prevailing snow conditions, obtaining reliable estimates of snow depth over lake and sea ice would be challenging using only X- and Ku-band backscattering information.

Keywords: remote sensing; synthetic aperture radar; sea ice; snow

1. Introduction

Snow cover has a major impact on the evolution of ice cover both in lake and sea environments [1,2]. During the freezing season, snow cover introduces a strong insulation effect that reduces ice growth at the ice/water interface. When the ice is thin, a heavy snow load on ice can contribute to the total ice mass by widespread surface flooding that forms slush and later snow-ice [2]. During the melting season, snow meltwater refreezing at the snow/ice interface leads to forming of superimposed ice [2]. Additionally, the high albedo of snow reflects a large part of solar radiation, which alters the surface energy balance and affects the amount of energy being reflected, absorbed, and transmitted through the ice and the underlying water. During the melt season, the ice starts to melt faster after snow melt-off [3].

Accurate snow depth data is needed to model the heat, momentum, and gas fluxes between the ocean, ice, and atmosphere [3]. Furthermore, snow on ice is a significant source of uncertainty in sea ice thickness estimation based on radar and laser altimetry (e.g. CryoSat-2 and ICESat-2) [4,5].

Snow depth on sea and lake ice needs to be observed with spatial and temporal resolutions required by numerical weather prediction models and operational monitoring of the state of lake and ocean conditions, e.g., daily with 10 km resolution. While accurate data can be obtained with in-situ observations, these rarely cover a large spatial extent at any one time. Airborne measurements of snow depth with an airborne Frequency-Modulated Continuous-Wave (FMCW) radar [6–8] cover a much larger area than in-situ measurements in a short time but are too expensive for continuous monitoring. Improved ultra wideband radars (UWBs) have also been installed in airplanes to find out the snow depth on the Arctic sea ice [9]. In addition, recently unmanned aerial vehicles (UAVs), known as drones, have been used to retrieve snow depth information on sea ice [10]. One solution is to use satellite microwave remote sensing data for the snow depth estimation on lake and sea ice [11,12].

There are some lake and sea ice properties, which have a large influence on the usability of microwave remote sensing instruments to obtain snow and ice information. In the case of lake ice, the water, ice and snow are non-saline, compared to sea ice and its snow cover, which can have a variable degree of salinity. The salinity has a large effect on the relative permittivity of snow and ice, and thus, on the penetration depth of electromagnetic waves. The relative permittivity $\varepsilon = \varepsilon' - j\varepsilon''$ is a complex parameter that characterizes the dielectric properties of media, where ε' is the dielectric constant and ε'' is the dielectric loss factor. The penetration depth is $\delta_p = \sqrt{\varepsilon'}/(k_0\varepsilon'')$, where $\varepsilon'' \ll \varepsilon'$ and k_0 is the wave number in free space. ε'' for sea ice is typically higher than for lake ice due to salinity inclusions, reducing the penetration depth greatly, when the frequency is less than 10 GHz [13]. For lake ice the penetration depth is larger, which results in also high frequency microwave (e.g. 36 and 89 GHz) data to carry snow and ice information from deep in the ice media. Ice dynamics, caused by winds and waves, are more substantial in the oceans than in the lakes, leading to drifting of sea ice, ice deformation and variable ice concentration, which yields more variable sensor signatures for sea ice than for lake ice. Over both lake and sea ice close to the coast the usage of the microwave radiometer (MR) data (resolution 5 to 25 km) is also limited due to mixed-pixel effects (i.e. mixture of land and ice signatures). Finally, the size of most lakes limits the feasibility of using the MR data in estimation of snow depth and other ice and snow properties to only the largest lakes [14].

In this study we investigate relationships between the snow depth on lake and sea ice and X- and Ku-band backscattering coefficients (σ^o) from synthetic aperture radar (SAR) imagery. The goal is to see whether snow depth estimation is possible with the σ^o data. Retrieval of sea and lake ice properties from X- and Ku-band backscattering was one of the secondary goals of the Cold Regions Hydrology High-Resolution Observatory (CoReH2O), a mission proposal in the ESA Earth Explorer program [15]. In the following we discuss about previous studies on snow depth and snow water equivalent (SWE) estimation on sea ice and lake ice using the MR and SAR data. We also discuss how sea ice and lake ice properties and σ^o are typically related. Finally, we present an overview of our study in Section 1.1.

Operational methods for snow depth (or SWE) estimation over sea ice with the MR data have been developed in many studies, e.g., [12,16,17]. Currently, the MR based snow depth data is accurate only over smooth first-year ice (FYI) [7,16,18,19]. Over deformed FYI or multiyear ice (MYI), snow depth is substantially underestimated [19]. The operational algorithms are typically based on the 19 GHz (K-band) and 37 GHz (Ka-band) brightness temperature (T_B) data and snow T_B signature difference between these two frequencies. Snow depth estimation accuracy is also in general degraded by mixture of various ice types typically present within large MR footprints. Snow depth on sea ice have been also investigated by using numerical one-dimensional snow and sea ice thermodynamic models, e.g. [20,21]. Recently, snow depth on sea ice has been estimated also by using satellite altimetry [22][23,24], for example, by using dual-frequency radar freeboards or coincident satellite radar and lidar altimetry. In the coming Copernicus Polar Ice and Snow topography Altimeter (CRISTAL) high-priority mission, a dual-frequency satellite altimeter will provide information about snow depth on sea ice and will also help to discriminate between the ice and snow interfaces [25]. Like for sea ice also for lake ice many studies on snow and ice properties and their temporal changes have been conducted using thermodynamic models, e.g. [26,27], and a Snow Microwave Radiative Transfer (SMRT) model [28]. Lake ice thickness has been studied using the satellite altimeter, moderate resolution imaging spectroradiometer (MODIS) and MR data, and in addition phenology studies have been conducted [14,29,30].

Products for the snow depth over Arctic sea ice retrieved from altimeter and MR satellite measurements as well as from reanalysis have been compared recently [31]. They highlighted the need for more targeted Arctic surveys with different spatial and temporal scales to be able to make more systematic comparison of airborne, in situ and satellite based observations. In a recent study, the CryoSat-2 altimeter measurements have been combined with passive microwave (AMSR) and infrared (AVHRR) measurements to obtain snow depth on sea ice [31].

In order to obtain information of snow depth at fine spatial scales (~0.1-1km), the use of SAR data, that has much better spatial resolution than MRs, has been investigated in some case studies, e.g. [32–34]. These have not yet resulted in any operational applications. So far, studies have been conducted mainly with C-band SAR sensors due to availability of large amount of SAR imagery. However, theoretical investigations indicate that the effect of snow cover on sea ice to radar backscattering at the X- and Ku-band can be more pronounced than at C-band [35–38].

There are several factors that influence the σ^o of a target – both the parameters of the SAR sensor and the properties of the target itself. Examples of the former are wavelength (frequency), polarization, incidence angle, and resolution, and of the latter are surface roughness (compared to the SAR wavelength), volume fraction, size, and shape of the scatterers in the media, and relative permittivities of the scatterers and the host media. In case of snow-covered lake and sea ice, snow depth, snow density, snow microstructure (e.g. crystal size), amount of liquid water in the snowpack and surface roughness contribute to the measured σ^o. These snow properties vary spatially and temporally as a result of snow transport by wind, melt-refreeze events, and snow deposition and metamorphism.

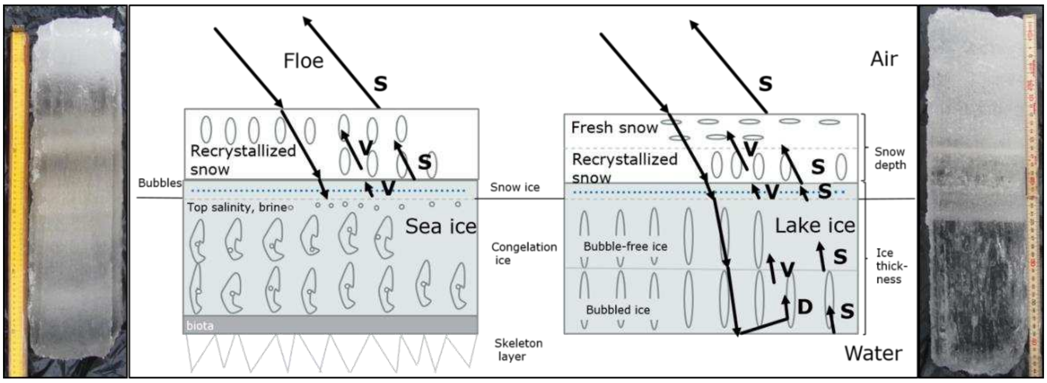

Figure 1. Main sources of radar backscattering (V for volume, S for surface and D for double-bounce scattering) for sea ice and lake ice environments. Radar wave penetration depth is dependent of ice salinity and temperature [12]. In sea ice, the penetration depth is much smaller due to salinity in ice. The ice core sample on the left was collected in Marjaniemi offshore Hailuoto on land-fast sea ice in the Baltic Sea. The ice core sample on the right was collected in Lake Orajärvi, Sodankylä, Northern Finland.

Different backscattering sources contributing to the measured σ^o for sea ice and lake ice are shown in Figure 1. These include surface scattering at the air-snow, snow-ice and ice-water interfaces, as well as scattering in the ice and snow volumes [39,40]. Typically, dry snow cover on ice increases σ^o compared to the case of bare ice through the increased backscattering in the snow volume [40,41]. For sea ice, the total σ^o typically consists of surface scattering from the snow surface, volume scattering from the snow layer, surface scattering from the ice surface and scattering from the air bubbles and brine pockets in the ice medium. For lake ice, there is more volume scattering from the lower layers of the ice, surface scattering from internal layers in the ice, scattering from the ice-water surface and double-bounce scattering from the bottom bubbled ice layer are included as well [42,43]. In recent studies, the scattering caused by the roughness of ice/water interface has been found to be the primary contribution to the total scattering over lake ice and not the double bounce from air bubbles, as has been assumed previously [29,44]. In the case of wet snow, the high dielectric contrast between air and wet snow causes scattering from the snow surface to become a dominant factor [40]. In case of rough ice, the effect of dry snow cover can be negligible, with the ice surface scattering being a dominating factor, especially in lower frequencies, e.g. at C-band [35,40].

An investigation using C-band SAR indicated that changes of the dielectric properties of snow cover due to an air temperature change are detectable in σ^o for smooth thick landfast FYI [32]. This allowed to detect SWE changes using SAR image pairs, one acquired in cold (~-26 °C) and one in moderately cold (~-14 °C) conditions. Snow cover affects the temperature of the upper surface of the ice, which affects the brine volume, dielectric properties and scattering characteristics within the snow volume [32]. In higher temperatures, the snow grains become brine wetted and produce volume scattering.

It has been found that even a thin snow cover (2 cm) increases σ^o at an oblique incidence angle at C- and Ku-bands [41]. However, increasing dry snow depth did not further influence σ^o [41]. On contrary to cold conditions (-7.9 °C), no relationship between various radar polarimetric parameters and snow depth was found under warmer conditions (-0.4 °C) [34]. The results suggested that snow depth estimation based on snow thermodynamics at warm conditions is not possible, whereas during cold winter conditions (<-10 °C), snow depth could be retrieved from SAR data. In general, for sea ice σ^o at the C-band, volume or mixed scattering components increase with increasing snow depth, most likely due to brine-wetted snow layers at the ice-snow interface [34].

Investigations using higher frequencies, such as X-band, show that the effect of snow cover on σ^o is large, especially in the case of FYI [35]. For lake ice, Ku-band σ^o, measured with ground-based scatterometers, has been found to be sensitive to the snowpack, whereas X-band σ^o was found to be largely insensitive [45]. Based on the scatterometer measurements, as the wavelength is shorter at Ku-band (17.4 mm) compared to X-band (31 mm), the interaction with initial tubular bubble formation (see Figure 1) close to the ice/water interface and with grains within the snowpack above the ice may be increased [46].

SAR imagery has been also used for lake ice classification (open water and various ice types, ice break-up) and to detect floating and bedfast lake ice regimes in the Arctic, e.g. [47–50]. In addition, using polarimetric decomposition in order to understand scattering processes in freshwater ice has been investigated recently [51].

Finally, a comprehensive review of the remote sensing of lake and river ice presented nearly ten years ago by Duguay et al. [52] stated that to their knowledge no operational method has yet been developed for estimating snow depth or SWE on lake ice. To our knowledge this is still the case.

1.1. Overview of the Study

The first objective in this paper is to investigate relationships between the snow depth on lake and sea ice and σ^o at the X- and Ku-bands. We use SAR and in-situ data collected in Finland, between February and March 2012, during Phase A studies of the CoReH2O mission [15]. The X- and Ku-band SAR data was acquired with ESA's airborne SnowSAR sensor [53]. Lake ice SAR and in-situ data were acquired on Lake Orajärvi, in Northern Finland, and sea ice data on smooth landfast ice in the Bay of Bothnia of the Baltic Sea, see Figure 2. The acquired airborne SAR data is compared with in-situ measurements collected along tracks on lake ice and sea ice. In particular, the relationships between spatial variability of snow depth and multi-channel σ^o signatures and various σ^o polarisation ratios are studied. The second objective is to investigate relationships between temporal evolution of snow depth and σ^o. This study is conducted using time series of TerraSAR-X (TSX) Stripmap Mode images (VV- i.e. vertical-vertical- and VH- i.e. vertical-horizontal- polarisations) acquired over the lake ice site in 2011-12. During this time an ice mass balance buoy (IMB) collected continuous snow and ice thickness data.

We note that although there are many other snow and ice properties besides snow depth contributing to the measured σ^o, such as snow grain size and the size, shape and density of ice air inclusions (i.e. bubbles). However, here we investigate empirically the relationship between snow depth and σ^o. This is due to interest to see if a simple σ^o value or ratio based snow depth estimation is possible with the acquired X- and Ku-band σ^o data. We know from past studies that grain size, bubbles, etc., need to be accounted for in order to e.g. accurately model the backscattering response; however, from the point of view of operational applications, acquiring any quantitative information on either one is very challenging, especially at high spatial resolution.

This paper is organized as follows. Materials and methods used in this study are first presented in Section 2. The results of our study are presented in Section 3, starting with an overview of snow and ice properties in the sea ice and lake ice sites, and followed by a quantitative analysis of multi-channel SnowSAR σ^o data against snow depth on lake and sea ice. Furthermore, a qualitative analysis of TSX imagery for lake ice and the time series of TSX σ^o over lake ice are presented. In Section 4 (Discussion), we compare our results to previous work, and finally, we give our conclusions in Section 5.

2. Materials and Methods

In the following, the study areas for sea ice and lake ice are first presented, followed by descriptions of acquired datasets and their processing for analysis.

2.1. Study Areas

2.1.1. Baltic Sea landfast ice test site

Sea ice test site was located on smooth landfast ice near Hailuoto Island in the Bay of Bothnia of the Baltic Sea, see Figure 2. The Baltic Sea is a semi-enclosed brackish sea water basin in Northern Europe. The duration of ice season is from five to seven months in the Bay of Bothnia where our test area was located. The upper limit for thermodynamically grown ice is around 70 cm during most winters, the measured maximum being 120 cm [54]. The salinity of the Baltic Sea ice is typically from 0.2 to 2 ‰ depending on the location, time, and weather history [55].

2.1.2. Lake Orajärvi test site

The lake ice test site was located on Lake Orajärvi, in Sodankylä, in Northern Finland, see Figure 2. Lake Orajärvi is a middle sized (10.95 km^2) freshwater lake. Typically, the duration of the ice season is from Nov/Dec to May/Jun (from six to eight months) [27]. The maximum ice thickness usually reaches more than 50 cm in late April [27]. Snow is present on the ice surface every winter season but its spatial distribution is variable across the lake. The mean snow depth and ice thickness during the winter season varied between approximately 2 and 43 cm, and 12 and 69 cm, respectively, in a multiyear study [27].

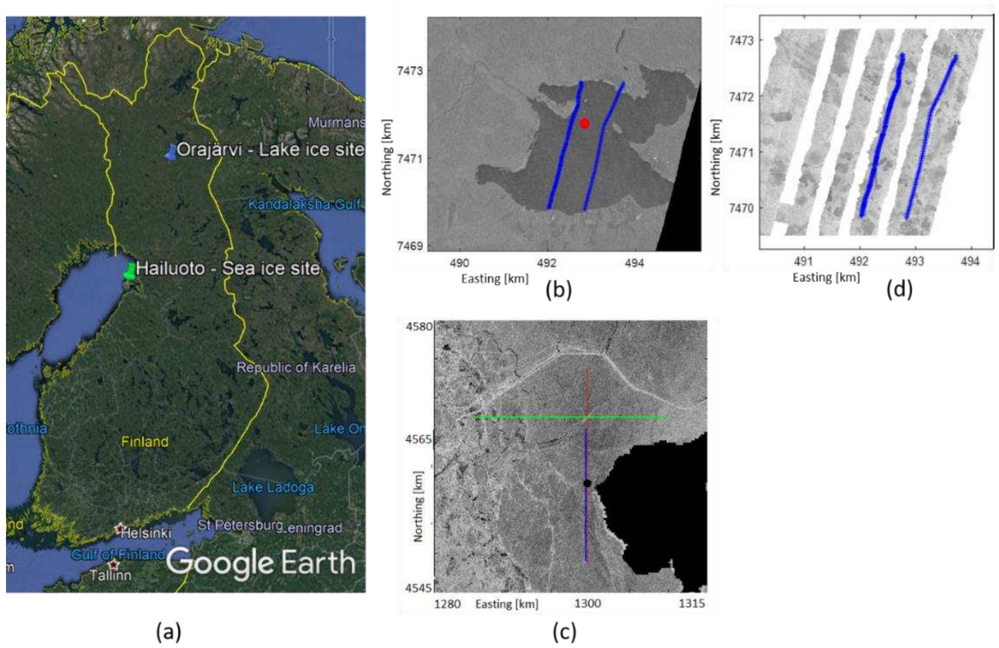

Figure 2. a) The study areas on the map of Finland (on Google Earth), b) Lake Orajärvi site on TSX image, VV polarisation. The location of an Ice Mass Balance buoy is marked with a red circle. In-situ

lines of the mission 4 are marked with blue lines. c) Baltic Sea landfast ice site on COSMO-SkyMed ScanSAR Wideregion HH-polarisation image acquired on 8 March 2012. Blue line shows in-situ measurement transect, and red and green lines are SnowSAR acquisition lines. Only the imagery along the red line is used in this study. d) SnowSAR KuVV imagery with in-situ measurement transects of the mission 4 on lake ice.

2.2. Data

2.2.1. Airborne SnowSAR Data

SnowSAR [53] operates simultaneously at the X- (9.6 GHz) and Ku- (17.25 GHz) bands with VV- and VH- polarizations (i.e. XVV, XVH, KuVV and KuVH). SnowSAR imagery was acquired at a spatial resolution of 2 m, swath width of around 400 m and mean antenna look angle of 40° [56]. Noise equivalent σ^0 is < -28 dB. The radiometric stability of σ^0 is < 0.5 dB, and the absolute bias is < 1 dB.

For the lake ice site, the SnowSAR data (σ^0 and elevation angle) from three missions are used here; for mission 2 one flight track in a SAR mosaic acquired on 9 January 2012 close to 14:30, local time (UTC+2h), for mission 4 two flight tracks in a mosaic acquired on 7 February 2012 close to 17:00, and for mission 5 one flight track in a mosaic acquired on 22 February 2012 close to 14:00. These flight tracks were approximately 7 km in length. A total of ten SnowSAR data acquisitions were flown over the area (see Table 1). However, there were only three acquisitions (missions 2, 4 and 5) that covered the lake ice areas and had enough coincident in-situ data (more than 10 datapoints) to perform an analysis. In the timeseries analysis, airborne SnowSAR data from all the missions (missions from 1 to 10), over Lake Orajärvi, are used.

Table 1. SnowSAR flight days and in-situ dates for each mission and the closest TerraSAR-X image.

Mission	SnowSAR flight date ****	In-situ date	TSX date (closest image)
1	19.12.2011 20.12.2011	19.12.2011 20.12.2011	17.12.2011
2 *	**09.01.2012** 10.01.2012	09.01.2012 **10.01.2012**	8.1.2012
3 *	23.01.2012 24.01.2012	23.01.2012 **24.01.2012**	30.1.2012
4 *	**07.02.2012** 08.02.2012	07.02.2012 **08.02.2012** **09.02.2012***	10.2.2012
5 *	**22.02.2012** 23.02.2012	**22.02.2012** 23.02.2012 24.02.2012	21.2.2012
6 **	26.2.2012	25.02.2012 26.02.2012	21.2.2012
7 ***	01.03.2012	29.02.2012 **01.03.2012**	3.3.2012
8 ***	05.03.2012	**05.03.2012**	3.3.2012
9 ***	10.03.2012	**08.03.2012** 13.03.2012	14.3.2012
10 *	24.03.2012	**23.03.2012**	25.3.2012

* Snowpits on lake ice; ** No in situ points on lake ice; *** Some in situ points on lake ice (N < 10); **** In situ tracks on lake ice (in the column marked with grey).

SnowSAR imagery over the landfast sea ice site was acquired along a 25 km track from south to north near Hailuoto Island, see Figure 2(c). The acquisition time was on 8 March 2012 between 13:00 and 14:00, local time.

2.2.2. TerraSAR-X Data over Lake Orajärvi

Over the Lake Orajärvi, TSX Stripmap Mode imagery at repeat-pass orbits were acquired between October 2011 and May 2012. The total number of images is 23, with a temporal spacing of 11 days. The Stripmap images were acquired at VV- and VH-polarisations, with a native resolution of ~2.5 m. For the TSX data, the noise equivalent σ^o is typically -22 dB and the range of incidence angle is from 33.14° to 34.44° [57]. The radiometric stability for TSX is better than 0.15 dB.

2.2.3. In-Situ Data on Lake Orajärvi

On the Lake Orajärvi, in-situ data for the mission 2 was acquired on 10 January 2012, one day after the SnowSAR imagery acquisition, along one transect with a length of around 4 km. Snow depth was measured with the Magnaprobe instrument (see http://snowhydro.com) in 269 locations (measured once in approximately every 15 meters) [58]. Ice thickness, snow density and SWE were measured in five locations. In addition, SWE was measured in three locations. Unfortunately, the closest snow pit measurement was on 8 February.

In-situ data for the mission 4 was acquired on 8 February 2012, one day after the SnowSAR imagery acquisition, along two transects (denoted as track1 and track2) with a length of around 3 km, see Figure 2(d). Snow depth was measured with the Magnaprobe instrument in 254 locations (measured once in approximately every 20-30 meters) [58]. Ice thickness, snow density and SWE were measured in four locations. In addition, snow pack stratification, snow density, temperature, volumetric wetness (moisture), grain size and grain type profile were measured in a single snow pit on 9 February. A snow fork was used for the moisture measurements.

In-situ data for the mission 5 was acquired on 22 February 2012, on the same day as the SnowSAR imagery acquisition, along one transect with a length of around 3 km. Snow depth was measured in 1086 locations (measured once in approximately every 3-4 meters). Ice thickness, snow density and SWE were measured in six locations and mere SWE in two locations. In addition, snow pack stratification, snow density, temperature, moisture, grain size and grain type profile were measured in a single snow pit on 22 February.

Weather data was available from an automatic weather station (AWS) 7.7 km west of the lake ice site in the Sodankylä Arctic Space Centre of the Finnish Meteorological Institute (FMI).

An Ice Mass Balance Buoy (IMB) was deployed on Lake Orajärvi (67 21.704’ N, 26 50.047’ E, see Figure 2(b)). The buoy measured a vertical temperature profile from air to water through snow and ice using a thermistor string with 2 cm spacing of sensors. The measurements were conducted four times a day during Dec 2011 – Apr 2012. The time series of snow depth and ice thickness were derived from the temperature profile data [27].

2.2.4. In-Situ Data on Landfast Ice

For the landfast sea ice test site, in-situ data was gathered along a transect from south to north during 7 – 8 of March 2012. The length of the transect was 15.2 km. Measured in-situ data included snow depth measured once in every 100-200 meters, SWE and sea ice thickness and freeboard at every 1 km. In addition, the scale of local snow depth variation was determined using two 10 meter transects with a 1 meter sampling interval. Two ice cores were sampled for sea ice salinity determination. The general structure of the snowpack was observed visually. Snow depth was measured either with a measuring rod or a snow scale, while SWE was measured using the snow scale. Weather data was available from the nearby FMI Marjaniemi AWS in the Hailuoto Island.

Unfortunately, the in-situ samples are not completely covered by the SnowSAR acquisition swath. Only about 20 measurement points out of 87 were in the area of the SnowSAR image covering 2.4 km of the total in-situ transect.

2.3. Methods

2.3.1. SnowSAR and TerraSAR-X Data Processing

The SnowSAR images were orthorectified into the UTM35 coordinate reference system and sampled to a 2 m grid. The co-location of the X- and Ku-band SAR images was studied by comparing to other datasets from the area, such as LiDAR data provided by the National Land Survey of Finland and Corine Land Cover classification data provided by the Finnish Environment Institute. The geometric accuracy of the SAR data was found to be within 5 m.

For the sea ice site, σ^0 data windows of size 5 by 5 pixels around each of the 20 in-situ samples covered by the SnowSAR images were extracted. Mean σ^0 was then calculated for each window. Larger window sizes were also tested, e.g. 50 by 50 (i.e. 100 m x 100 m), but the relation between mean σ^0 and snow depth was deteriorated for larger windows. Also median σ^0 from the window was tested but it had poorer relationship with the snow depth than the mean σ^0.

For lake ice an averaging window of size 5 by 5 pixels around each in-situ sample was also used. However, due to some visible artefacts in the SAR images, such as snow mobile tracks from in-situ measurements shown as line of increased σ^0, the following filtering with the 5 by 5 window was conducted: The average and 1*std (2*std also tested) of σ^0 were first calculated. Then, pixels with a σ^0 value outside the avg±std (avg±2*std also tested) interval were rejected before the final σ^0 averaging within the 5x5 window. In addition, in-situ samples too close to an adjacent SnowSAR flight track in the mosaic were eliminated from the calculations.

Compensation of the radar incidence angle was performed using the cosine normalization method in order to reduce the influence of the incidence angle on the mean σ^0 [39]

$$\sigma^0_{\theta_{ref}} = \frac{\sigma^0 \cdot \cos^2\theta_{ref}}{\cos^2\theta}, \quad (1)$$

where $\sigma^0_{\theta_{ref}}$ is the normalised σ^0, σ^0 is the original backscattering coefficient, θ is the original incidence angle and θ_{ref} is the reference angle to which the normalisation is conducted. The data was normalized to the reference incidence angles 43.8° and 43° for the Ku- and X- band data, respectively, as the antennas for the Ku- and X-bands were designed to look at the target at those center angles. In the following Sections $\sigma^0_{\theta_{ref}}$ is referred shortly with σ^0.

The TSX Stripmap images that were acquired at VV- and VH-polarisations, with a native resolution of ~2.5 m, were also re-sampled to the 2-m UTM35 grid.

2.3.2. Comparison of SnowSAR backscatter and In-situ Data

The measured snow depths were compared with the mean σ^0 values of the SnowSAR bands XVV, XVH, KuVV and KuVH, and various two-channel ratios of the mean σ^0 e.g., KuVV/XVV, KuVV/KuVH. It is hypothesized that the channel ratios should be more sensitive to the spatial variations in snow depth, as σ^0 changes depend on both the polarization and frequency. For example, at the Ku-band volume scattering from snow is typically assumed to be larger than at the X-band, and backscattering at the VH-polarization is only due to the multiple scattering, but at the VV-polarization single scattering is dominating [40]. Over sea ice, the ratios involving the VH-polarization are likely somewhat contaminated by the overall low level of σ^0 close to the SnowSAR noise floor (< -28 dB). The investigated relationships between the snow depth and SnowSAR data are characterized by a linear regression fit which was selected instead of higher order fits due to large scatter in the datasets.

For the lake ice site, for the mission 4, the dependencies were investigated for the two SnowSAR tracks separately. This is due to different incidence angles between them. Although the data was compensated for the same incidence angle, the overlapping areas of the transects may have different σ^0 vs. snow depth relationships due to differing measurement geometries. In addition, results for the combined tracks were given.

2.3.3. TerraSAR-X and Ice Mass Balance Buoy Data

The changes in the average σ^0 values of the Lake Orajärvi were investigated qualitatively from the TSX images. The temporal evolution of the average σ^0 value of the entire lake was analyzed and compared visually with the TSX images. The average σ^0 was calculated from the area covered by Lake Orajärvi in each TSX image by using a mask from Corine data.

The time series of the TSX σ^o data from the IMB location and the IMB snow depth data were used to investigate relationships between the temporal evolution of the snow depth and σ^o.

In addition, the time series of air temperature, rainfall intensity and snow depth data from the closest AWS were added to the analysis to be able to compare their trends with the TSX σ^o and IMB snow depth during 1 Oct 2011 – 30 May 2012. The time series of the IMB temperature fields inside the snow and lake ice as well as the average temperature inside the snow pack as function of time were also calculated. The time series of different temperature layers inside the snow pack were studied in relation with the TSX σ^o time series.

3. Results

Here we present first an overview of snow and ice properties in the sea ice and lake ice sites. Next, relationships between the SnowSAR data and the snow depth on lake ice and sea ice are investigated and quantified. This is followed by qualitative analysis of the TSX imagery for lake ice, and analysis of the lake ice TSX σ^o timeseries.

3.1. Overview of Snow and Ice Properties in the Sea Ice and Lake ice Sites

Various snow and ice properties: snow depth, ice thickness, ice salinity, SWE and snow density, are listed in Table 2 for the sea ice and lake ice sites.

Table 2. Statistics of snow and ice properties for the sea ice and lake ice sites. For lake ice, the values are from the data, where coinciding SnowSAR data were available.

Sea ice	**Snow and ice properties**		
	VARIATION	MEAN	STD
Snow depth (cm) *	1 – 37 (2 – 19) **	14 (11)	7.4 (5.1)
Ice thickness (cm)	29 – 52	35	5.4
Ice salinity (ppt)	0.2 – 1.0	-	-
SWE (mm)	16 – 95 (25 – 44)	-	-
Snow density (g/cm^3)	0.28 – 0.36 (0.28 –0.34)	0.33	0.03
Mission 2 **Lake ice track**	**Snow and ice properties**		
	VARIATION	MEAN	STD
Snow depth (cm)	0.4 - 27	13	5.1
Ice thickness (cm)	20-30	25	3.8
Mission 4 **Lake ice track1**	**Snow and ice properties**		
	VARIATION	MEAN	STD
Snow depth (cm)	14 – 35	22 [21] ***	4.1 [4.1]
Ice thickness (cm)	38 – 40	39	1.0
Mission 4 **Lake ice track2**	**Snow and ice properties**		
	VARIATION	MEAN	STD
Snow depth (cm)	11.5 – 32	20	3.9
Ice thickness (cm)	-	-	-
Mission 5 **Lake ice track**	**Snow and ice properties**		
	VARIATION	MEAN	STD
Snow depth (cm)	21 – 41	30	3.5
Ice thickness (cm)	37 - 40	39	1.0

* The STD from local snow depth measurements of two 10 m snow depth transects measured at 1 m spacing was 9.3 cm i.e. showed large local variation in snow depth. ** In parentheses are shown the values for only that part of the in-situ transect, where coincident SnowSAR data were available. *** In brackets are shown the values for the track1 and track2 combined.

For the sea ice site, although the snow depth exhibited large spatial variability (compared to the mean), the average snow pack was relatively thin, only 11 cm. The snow and ice thickness in the sea ice site were within a typical range for the landfast ice in the Bay of Bothnia in early March [59]. The variation of snow density was within expected values for settled snow (0.2 to 0.3 g/cm^3) and wind packed snow (0.35 to 0.4 g/cm^3) [60]. Based on the in-situ observations, the structure of the snowpack was fairly homogeneous. There was a ca. 3 cm layer of hard crust on top with a layer of fine grained dry snow underneath. The snow was not frozen to the ice surface, but loose. The two sampled ice cores showed vertical salinity variations between 0.2 and 1.0 ppt which are typical low salinity values for sea ice in the Bay of Bothnia [55]. According to the AWS observations a few kilometers from the measurement line, the air temperature (T_a) was on average -3.7 °C during the SnowSAR data acquisition over the sea ice site on 8 March, and from -6.1 °C to -2.7 °C during the in-situ measurement campaign 7 - 8 March (-8 °C during the night between). The snow pack on the sea ice was qualitatively observed to be dry (i.e. volumetric wetness close to 0%).

For the lake ice site, in the mission 2, snow depth varied between 0.4 and 27 cm. According to the AWS data T_a was about -24 °C during the SnowSAR data acquisition on 9 January (daily mean -20.4 °C) and during the in-situ measurement campaign on 10 January the daily mean T_a was -12.6 °C. Based on the snow pit measurements on 8 December 2011 (the closest one for the mission 2), snow depth was 7 cm, the temperature of snow was between 0.4 (bottom) and -1.3 °C (top), the density was between 0.13 and 0.15 g/cm3, grain size approximately between 0.5 and 1.5 mm, and grain type was precipitation particles/needle on top and rounded grains/irregular on bottom part of the snow cover.

For the lake ice site, in the mission 4, snow depth varied between 12 and 35 cm. T_a was about -29 °C during the SnowSAR data acquisition on 7 February (daily mean -31 °C), and during the in-situ measurement campaign on 8 February the daily mean T_a was -26 °C. Based on the snow pit measurements on 9 February, snow depth was 20 cm, the temperature of snow was between -1.9 (bottom) and -17.4 °C (top), the density was between 0.05 and 0.21 g/cm3, moisture between 0.4 and 1.0 %, grain size approximately between 0.8 and 2.5 mm, and grain type was precipitation particles/stellars/dendrites/irregular on top and hollow cups on bottom part of the snow cover. The measured snow density values are typical for the site [61].

For the mission 5 snow depth varied between 21 and 41 cm. T_a was about -6 °C during the SnowSAR data acquisition on 22 February, and during the in-situ measurement campaign on 22 February the daily mean T_a was -9.6 °C. The snow pit measurements on 22 February showed snow depth of 30 cm. The temperature of snow was between -0.3 (bottom) and -13.9 °C (top), the density was between 0.14 and 0.24 g/cm^3, moisture 1 %, grain size approximately between 0.5 and 2 mm, and grain type was partly decomposed precipitation particles on top and hollow cups on bottom part of the snow cover.

T_a's during the SnowSAR flights and in situ data collection had the largest difference in the mission 2, where the former was approximately -20.4 °C and the latter -12.6 °C. For the mission 4, T_a's were -31 and -26 °C (for the track 1), respectively. The SnowSAR and in situ data for the mission 5 were acquired on the same day, thus T_a's were quite similar.

In the IMB time series from Dec 2011 to Apr 2012 the snow depth varied between 10 and 30 cm. The ice thickness varied between 16 and 58 cm.

3.2. SnowSAR Data versus Snow Depth on Lake Ice

The relation between the mean σ^o and the snow depth for the two measurement lines (track1 and track2 in the mission 4) was investigated separately. Figure 3 shows scatterplots between the snow depth and the mean σ^o at the four SnowSAR channels. Figure 4 has scatterplots between the SnowSAR channel ratios and snow depth for the track1. Linear regression fits to the data are also depicted in the figures. Statistics describing the linear regression between the σ° channels or channel ratios and the snow depth for the track1, track2 and for the both tracks combined are presented in Table 2.

For the track1, the coefficient of determination (R2) between the KuVV σ° and snow depth was modest, 0.33, but the p-value for the regression was <0.001. For the track2, R2 in the case of the KuVV σ° was only 0.19. In general, the results for the track2 show R2's than the track1, possibly because the track2 exhibited (by visual analysis of the SAR imagery) a wider variety of different lake ice types (mainly refrozen ice from cracks and leads).

The best sensitivity to the snow depth with all channels, in terms of R2, was found for the XVH σ° (R2=0.36 for the track1 and R2=0.24 for the track2), and within all channel ratios for the KuVV/KuVH ratio (R2=0.14 for the track1, R2=0.09 for the track2). For the combined tracks, the best sensitivity was again for the XVH (R2=0.29), but now for the KuVH/XVH ratio (R2=0.08). At XVH, σ° was found to increase more in relation to the snow depth (0.16 dB/cm for the track1 and track2, and for the combined tracks) than at other channels.

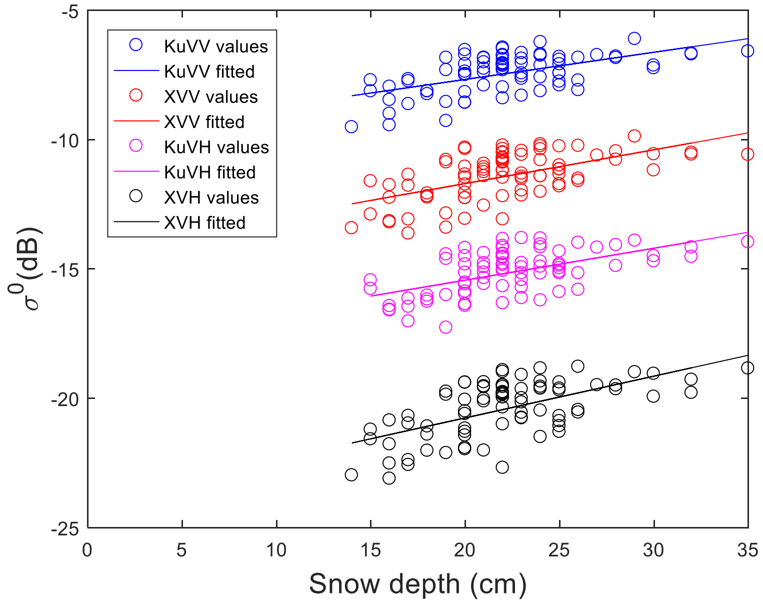

Figure 3. SnowSAR X- and Ku-band backscattering coefficients as a function of snow depth on the Lake Orajärvi for the track1 in the mission 4. The σ° was scaled to the reference incidence angle of 43.8 deg for the Ku-band and 43 deg for the X-band.

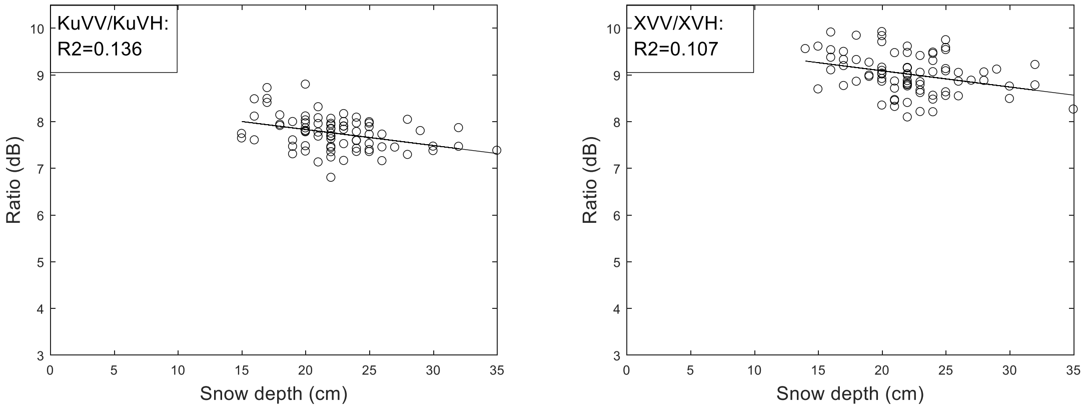

(a) (b)

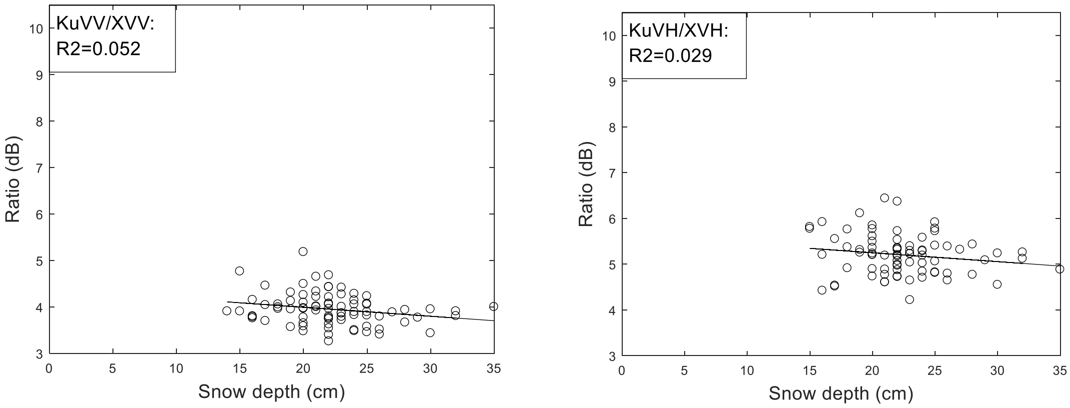

(c) (d)

Figure 4. SnowSAR channel ratios as a function of snow depth on the Lake Orajärvi for the track1 in the mission 4; (a) KuVV/KuVH, (b) XVV/XVH, (c) KuVV/XVV and, (d) KuVH/XVH. Linear regression fits and coefficient of determination (R2) are also shown. The σ^0 was scaled to the reference incidence angle of 43.8 deg for the Ku-band and 43 deg for the X-band.

Table 3. Statistics of the linear regression between the SnowSAR backscattering coefficient data and the in-situ snow depth data for the mission 4 track1, track2 and both tracks combined in the lake ice site.

Lake Track1				
	SLOPE TERM [DB/CM]	AVERAGE [DB]	R2	P-VALUE
XVV	0.13	-11.3	0.34	< 0.001
XVH	0.16	-20.3	**0.36**	< 0.001
KuVV	0.11	-7.4	0.33	< 0.001
KuVH	0.12	-15.1	0.33	< 0.001
KuVV/KuVH	-0.03	7.8	**0.14**	< 0.001
XVV/XVH	-0.03	9.0	0.11	0.003
KuVV/XVV	-0.02	4.0	0.05	0.042
KuVH/XVH	-0.02	5.2	0.03	0.138
Lake Track2				
	SLOPE TERM [DB/CM]	AVERAGE [DB]	R2	P-VALUE
XVV	0.08	-12.7	0.15	< 0.001
XVH	0.16	-21.1	**0.24**	< 0.001
KuVV	0.08	-8.5	0.19	< 0.001
KuVH	0.12	-14.3	0.22	< 0.001
KuVV/KuVH	-0.04	6.0	**0.09**	< 0.001
XVV/XVH	-0.07	8.6	0.07	< 0.001
KuVV/XVV	-0.01	4.3	0.01	0.142
KuVH/XVH	-0.04	6.8	0.06	0.002
Tracks combined				
	SLOPE TERM [DB/CM]	AVERAGE [DB]	R2	P-VALUE
XVV	0.12	-12.2	0.26	< 0.001
XVH	0.16	-20.8	**0.29**	< 0.001
KuVV	0.11	-8.1	0.27	< 0.001
KuVH	0.10	-14.6	0.18	< 0.001
KuVV/KuVH	-0.00	6.6	0.00	0.722
XVV/XVH	-0.03	8.7	0.02	0.016
KuVV/XVV	-0.02	4.2	0.06	< 0.001

KuVH/XVH	-0.05	6.3	**0.08**	< 0.001

Additional, quick tests were conducted for images (5x5 mean averages) for the missions 2, 4 and 5 (see Table 4). For the mission 4, similar but somewhat different relations were found compared to the previous ones, due to the more simple analysis performed here (e.g. no angle compensation or std filtering used). However, none of the investigated relations between the SnowSAR channels or channel ratios were found to be statistically significant.

Table 4. Statistics of the linear regression between the SnowSAR backscattering coefficient data and in-situ snow depth for missions 2, 4 and 5 (based on quick analysis).

	Mission 2				**Mission 4**			
Polarisation	R2	P-VALUE	SLOPE TERM [DB/CM]	DEVIATION	R2	P-VALUE	SLOPE TERM [DB/CM]	DEVIATION
XVV	0.04	0.009	-0.058	0.0221	0.26	< 0.001	0.2089	0.0223
XVH	0.04	0.016	-0.066	0.0275	**0.37**	< 0.001	0.2608	0.0216
KuVV	0.06	0.002	-0.099	0.0317	0.25	< 0.001	0.1899	0.0207
KuVH	0.05	0.005	-0.113	0.0398	0.24	< 0.001	0.1714	0.0190
KuVV/KuVH	0.01	0.224	0.013	0.0102	0.01	0.230	0.0185	0.0154
XVV/XVH	0.01	0.201	0.010	0.0076	0.04	0.001	-0.0519	0.0158
KuVV/XVV	0.04	0.016	-0.042	0.0171	0.03	0.005	-0.0190	0.0067
KuVH/XVH	0.03	0.039	-0.047	0.0225	**0.14**	< 0.001	-0.0894	0.0138

	Mission 5			
Polarisation	R2	P-VALUE	SLOPE TERM [DB/CM]	DEVIATION
XVV	0.00	0.770	-0.003	0.0110
XVH	0.00	0.044	-0.024	0.0130
KuVV	0.00	0.397	-0.012	0.0144
KuVH	0.00	0.440	-0.012	0.0158
KuVV/KuVH	0.00	0.996	0.000	0.0046
XVV/XVH	0.02	< 0.001	0.021	0.0055
KuVV/XVV	0.00	0.045	-0.012	0.0062
KuVH/XVH	0.00	0.213	0.009	0.0074

Finally, similar analysis was conducted for the missions 2 and 5 as conducted for the mission 4 in Figures 3 and 4. The results are presented in Appendix A. The Figure A4 in Appendix A show that the best correlation can be found in the mission 4. The datasets in different missions differ in the sense that the snow depths cover different ranges. The snow depths in the mission 2 include mostly small values, the mission 5 large values and the mission 4 between those values.

The level of backscattering in the mission 5 is lower than in the mission 4, especially at the Ku band. The correlation seems to be better between approximately 14 cm – 25 cm, than with smaller or larger snow depths. The reason could be that in small snow depths the effect of ice under the snow is dominating, and in larger snow depths the double bounce effect from the bottom of the ice is lost.

In the mission 4, the standard deviation of ice thicknesses is smaller (approximately 1 cm, see Table 2) than in the mission 2 (approximately 4 cm), suggesting that the ice could be more like level ice and the surface roughness might not be as large as in the mission 2.

3.3. SnowSAR Data versus Snow Depth on Sea Ice

The in-situ samples for the sea ice site covered only partly the SnowSAR acquisition, see Section 2.2.4. Only 20 samples out of 87 are within the SAR swath area. Among these samples there were two points on smooth ice, one was located on a broken ice field, and two on ice ridges. The X- and Ku-band σ^{o} as a function of snow depth for the sea ice site is presented in Figure 5. The channel ratios

KuVV/KuVH and KuVV/XVV as a function of snow depth are shown in Figure 6. The statistics of the linear regression between the σ^0 data and snow depth are shown in Table 5.

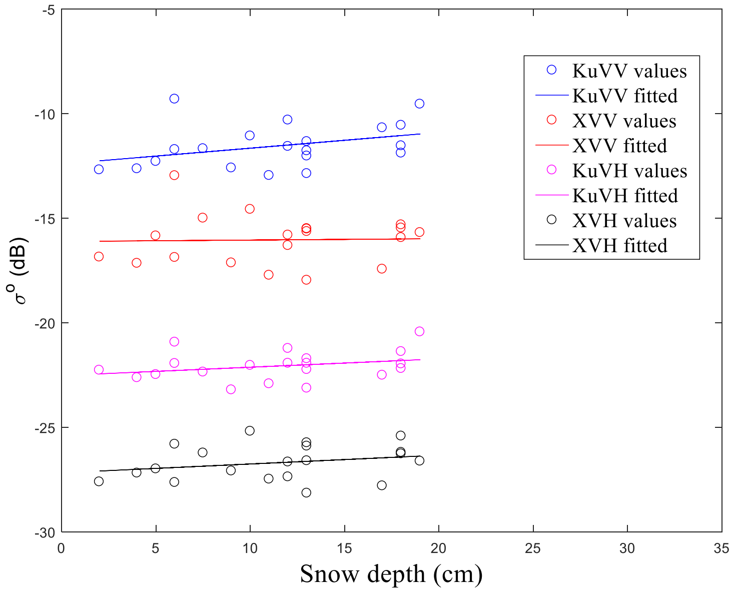

Figure 5. SnowSAR X- and Ku-band backscattering coefficients as a function of snow depth on landfast sea ice in the Bay of Bothnia. The σ^0 was scaled to the reference incidence angle of 43.8 deg for Ku-band and 43 deg for X-band.

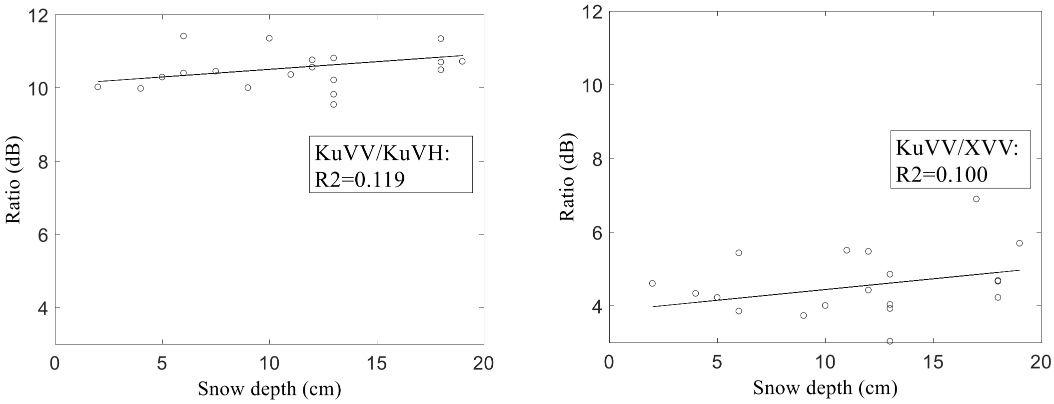

(a) (b)

Figure 6. (a) Snow depth vs. SnowSAR KuVV/KuVH and (b) snow depth vs. KuVV/XVV on landfast sea ice in the Bay of Bothnia. The σ^0 was scaled to the reference incidence angle of 43.8 deg for Ku-band and 43 deg for X-band.

At KuVV σ^0 was found to increase more in relation to snow depth (0.09 dB/cm) than in the case of XVV (0.04 dB/cm), KuVH (0.05 dB/cm) and XVH channels (0.05 dB/cm). However, at KuVV R2 is only 0.21. Larger σ^0 values were observed for KuVV than for XVV, this frequency behaviour is in line with previous studies, e.g. [35]. For XVH and KuVH the σ^0 variation within snow depth was diminished by the SnowSAR noise floor. The highest sensitivity to snow depth within the channel ratios was found for KuVV/KuVH, but the R2 value was only 0.12.

The σ^0 data scatter was too large and the data amount too small for reliable conclusions about the behavior of either individual channels or the ratios as a function of the snow depth. The p-value of the linear regression was significant only for KuVV. In Figure 6(b), KuVV/XVV slightly increases with increasing snow depth which can be explained by larger increase of snow volume scattering at the Ku- than at the X-band. The increase of KuVV/KuVH with increasing snow depth in Figure 6(a) could suggest larger increase of single scattering in snow volume than that of multiple scattering as a function of the snow depth. However, other variables such as snow density and grain size can also influence the σ^o value. Unfortunately, our data set did not allow to study their effect on the σ^o.

It is worth noticing that T_a during the SnowSAR image acquisition was -3.7 °C on the average. Some earlier studies indicate that if T_a is warmer than - 5 °C, there might be liquid water in the snow due to snow melt onset, and the backscatter can be largely attenuated, e.g. [62]. Therefore, possible liquid-water content in the snow may have decreased the σ^o values.

Table 5. Statistics of the linear regression between the SnowSAR backscattering coefficient and snow depth data for the sea ice site.

SnowSAR band	**Line regression statistics**			
	SLOPE TERM	**OFFSET**	**R2**	**P-VALUE**
XVV	0.04	-15.3	0.02	0.545
XVH	0.05	-26.2	0.07	0.280
KuVV	0.09	-11.5	**0.21**	0.042
KuVH	0.05	-21.6	0.12	0.130
KuVV/KuVH	0.04	10.1	**0.12**	0.137
XVV/XVH	-0.01	10.8	0.10	0.692
KuVV/XVV	0.06	3.9	0.10	0.175
KuVH/XVH	0.01	4.6	0.00	0.881

3.4. Analysis of TerraSAR-X Imagery Time Series on Lake Ice

3.4.1. Qualitative analysis

TSX satellite StripMap imagery at VV- and VH-polarization over the Lake Orajärvi, covering the time period from October 2011 to May 2012 was applied to analyze the variability of the X-band σ^o signatures over time. In Figure 7, all TSX σ^o images at VV-polarization are shown. In the images distinct seasonal changes can be observed: after initial low σ^o typical for calm open water, a first sharp increase in σ^o can be observed on 14 November. At this time, ice was not yet formed on the lake, and the high σ^o originated from waves caused by winds, as rough water surface areas have high σ^o [39]. The wind speed was 2.7 - 7.2 m/s (from light to moderate) and 5.4 -13.8 m/s (from gentle to strong) in gusts.

The following TSX acquisition on 25 November shows again a low σ^o. During this acquisition, new, level congelation ice covered almost the entire lake forming a highly specular surface with low backscatter characteristics. During the following acquisitions on 6, 17 and 28 December, the observed average σ^o gradually increases, with the increasing of σ^o concentrating around cracks and leads visible on the ice surface. Subsequent overflow of water on the ice surface, and formation of a snow-ice layer causes these areas of increased σ^o to gradually expand and eventually cover the whole area of the lake. During the cold winter period, metamorphism in ice and snow cause gradual spatial changes in σ^o. In the spring acquisitions, on 16 and 27 April, σ^o drops as a result of warming weather and subsequent wetting of snow on top of the ice. σ^o increases again for acquisitions on 8 and 19 May, as lossy and highly specular wet snow is merged in the melting ice beneath [63]. In the acquisition on 19 May, shorelines of the lake can be seen in the SAR image to be already free of ice. After that the ice melts quickly due to warm weather and the absence of snow on the ice, with the lake largely being ice-free in the last acquisition on 30 May.

The findings above suggest several possibilities to monitor the seasonal evolution of lake ice in the Northern Europe using X-band SAR; including the onset and break-up of ice cover, wetting of the ice/snow surface, ice deformation, cracking, and slushing events. The high spatio-temporal variability of σ^o also explains some of the difficulties in associating snow conditions on lake ice directly with the σ^o data. Previous studies of lake ice phenology have mostly used C-band SAR and QuickSAT Ku-band scatterometer data and have focused on the Arctic regions [52].

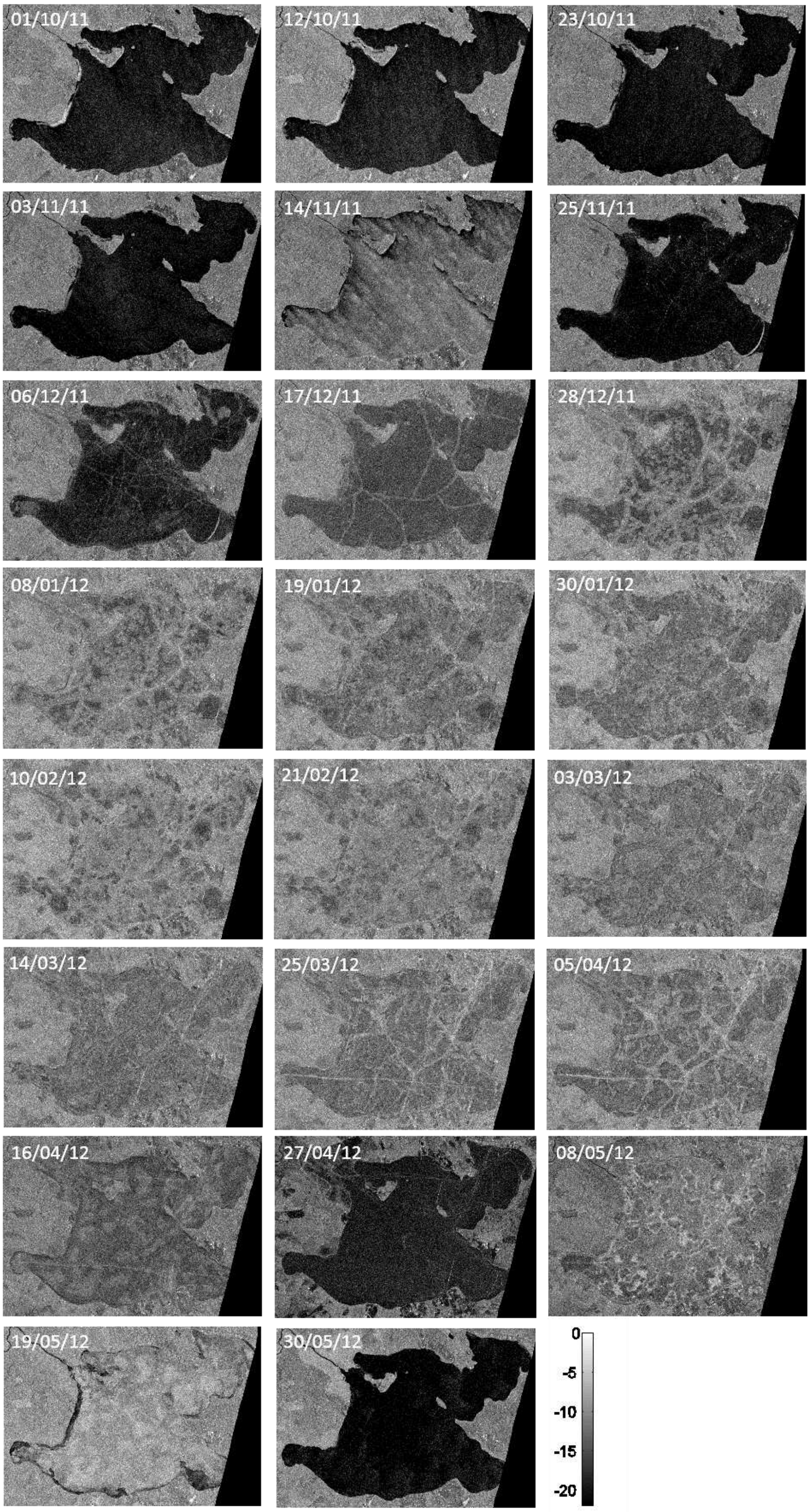

Figure 7. TSX SAR images at the X-band VV- polarization over the Lake Orajärvi in 2011-2012. The TSX image from 8 January 2012 is closest to the mission 2. The TSX images from 10 and 21 February 2012 are closest to the missions 4 and 5, respectively.

3.4.2. Time series of TerraSAR-X mean σ^o over Lake Ice

Figure 8 depicts the time series of the observed average TSX and SnowSAR σ^o at VV- and VH-polarisations with boxplots over the Lake Orajärvi. In addition, mean σ^o of TSX at IMB location for VV and VH polarisations are shown. The closest TSX data in the mission 2 is from one day before the SnowSAR flight and two days before the in situ data. For the mission 4, the closest TSX data is from three days after the SnowSAR flight and one to two days after the in situ data. The closest TerraSAR data in mission 5 is from one day before the SnowSAR flight and the in situ data. Especially in Mission 4, there is a gap between the time of SnowSAR data and TSX data acquisition.

For TSX, the seasonal variation of the σ^o is larger at the VV- than at the VH-polarisation, but at VH low signal-to-noise ratio has limited the variation. The noise equivalent TSX σ^o is typically -22 dB [57]. The temporal TSX σ^o trends at VV and VH are similar. For SnowSAR as well, the temporal σ^o trends at VV and VH are quite similar, although at VH the σ^o values for the Ku and X bands are more apart from each other. The trend of the Ku band σ^o is opposite to the X-band σ^o during 19 December 2011 - 10 January 2012; 22 February 2012 - 26 February 2012 and 01 March 2012 – 05 March 2012 for both VV and VH. For the Ku-band the σ^o values are larger and there is more variation in the timeseries than at the X-band. When the X-band σ^o's for TSX and SnowSAR are compared, it can be seen, that in VH there is more difference as the values are more apart from each other although the trend is quite similar. There is a drop in the SnowSAR X-band timeseries on March 10, 2012 which is not that visible in the TSX ones. It should be noted, that there is less data for SnowSAR.

The difference between the SnowSAR measurements in the missions 2, 4 and 5, and the closest TerraSAR images were studied also by masking the SnowSAR image areas from the TerraSAR data. It didn't have much effect, especially in the mission 4. The use of that data would not give as good information about the temporal changes in the lake ice area, e.g. about the onset/offset of lake ice as the areas close to the shores would be excluded.

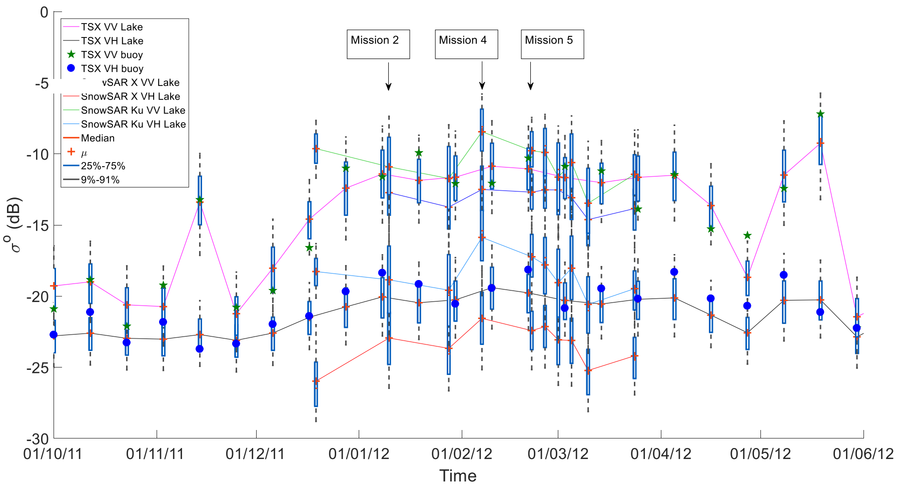

Figure 8. Time series of the average TSX and SnowSAR σ^o data at the VV- and VH-polarisations with boxplots from Lake Orajärvi in 2011-2012. In addition, mean σ^o of TSX at IMB location for VV and VH polarisations are shown as a green star and a blue circle, respectively.

The time series of the IMB snow depth data for the Lake Orajärvi is shown in Figure 9(a). In addition, T_a, rainfall intensity and snow depth from the closest AWS and the mean TSX σ^o at the IMB location for both VV and VH polarisations are shown. Unfortunately, the IMB dataset does not cover the end of April with advanced ice melting conditions. In Figure 9(b), the IMB snow depth, ice thickness and measured temperature fields inside the snow and ice are presented.

The timeseries of the TSX σ^o at the VV-polarisation shows that the σ^o is low in October, when the lake is still free of ice. During open water conditions σ^o rises occasionally due to waves, notably on 14 November when high winds induced visible wave patterns in the SAR image (see Figure 7). In mid-November, T_a drops below freezing, the lake ice starts forming and σ^o increases. The AWS snow depth increases as well. The onset of snow accumulation in the AWS snow depth data in Figure 9(a) coincides with the peak in the σ^o data series on 14 November.

During mid-winter, i.e. from December to March, σ^o is quite stable. Nevertheless, in two cases the σ^o decreases although the snow depth increases. As time goes on, the σ^o may increase due to recrystallization, i.e. reorganizing and growing of snow crystals [64].

The IMB snow depth varies between 9.7 cm and 30 cm and the σ^o at the VV-polarization during that period is between -13.9 dB and -9.9 dB. The ripple in the IMB snow depth data possibly indicates short term variations caused by, for example, snowfall and melting events, or by accumulation or erosion of snow due to wind. In the IMB data a sudden decrease in snow depth is visible in the end of February. A coinciding negative trend can be detected in the both VV- and VH-polarisation σ^o's. For the VV-polarisation σ^o there is a σ^o gradient of approximately -0.044 dB/day. For the IMB snow depth there is a gradient of -1.6 cm/day. The sudden decrease in the IMB snow depth might be caused by the increase in the amount of snow-ice (i.e. snow converting to ice) as observed in the in-situ measurements as well. The combined effect of extensive precipitation followed by high air humidity and cold T_a could have caused the formation of snow-ice to take place. Even if there was no actual melting of snow, the snow metamorphoses may cause compaction of snow. Whereas, the AWS snow depth continues to increase because there is no formation of snow-ice on land. From late March to the beginning of April, after the AWS T_a being above 0 °C, σ^o increases as T_a decreases, snow refreezes and granular snow creates more volume scattering, and presumably also due to growing snow depth.

When the melting season starts, σ^o starts to decrease as T_a increases above 0 °C in April. The wetter the snow becomes, the lower the σ^o values are. Later σ^o increases as snow on ice melts completely. Unfortunately, there is no IMB data for the end of April to investigate reasons for the decrease in σ^o. The onset of melting in the AWS snow depth data coincides with the drop in the VV-polarisation σ^o data series on 27 April. The time in the AWS snow depth data when all the snow has melted coincides the peak in the VV-polarisation σ^o data series on 19 May.

In general, an increase in T_a is seen as decrease in the TSX σ^o, i.e. those are inversely correlated (R2=0.18, p=0.05, when all TSX points are used; R2=0.54, p=0.0001, when two points with the lowest and the highest T_a's are excluded). In addition, the same kind of relation can be observed between T_a and the IMB snow depth; the snow depth is higher during the cold periods. Warmer ice temperatures in Figure 9(b), shown in colour of dark red, are probably caused by thicker snow layer [65] or generally warmer T_a at that moment.

Next, we investigate the influence of the temperatures inside the snow volume to σ^o. Layers of different temperatures within the snowpack were investigated more closely. As an example, the layer in snow having the temperature between -1.75 °C and -2.5 °C at 18:00 LT on the days of the TSX image acquisition is shown separately as a blue curve in the temperature field in Figure 9(b). It was found to be the most consistent temperature interval with the time series of the TSX σ^o data. After March, this consistency does not apply. Instead, the layer with the temperature between -5 °C and -10 °C is after the middle of March more valid.

It can be seen in Figure 9(a) and 9(b), that the days before the mission 4 were very cold (- 38.8 °C at the coldest on 5 February 2012) and several days without snowing until snowing new fresh snow just before the SnowSAR acquisition. The lake ice had also become thicker. In the mission 5 as well it has been snowing before the SnowSAR acquisition but T_a had not been as cold as in the mission 4. In the case of mission 2, snowfall was not detected between the SnowSAR acquisition and the collection of in situ data.

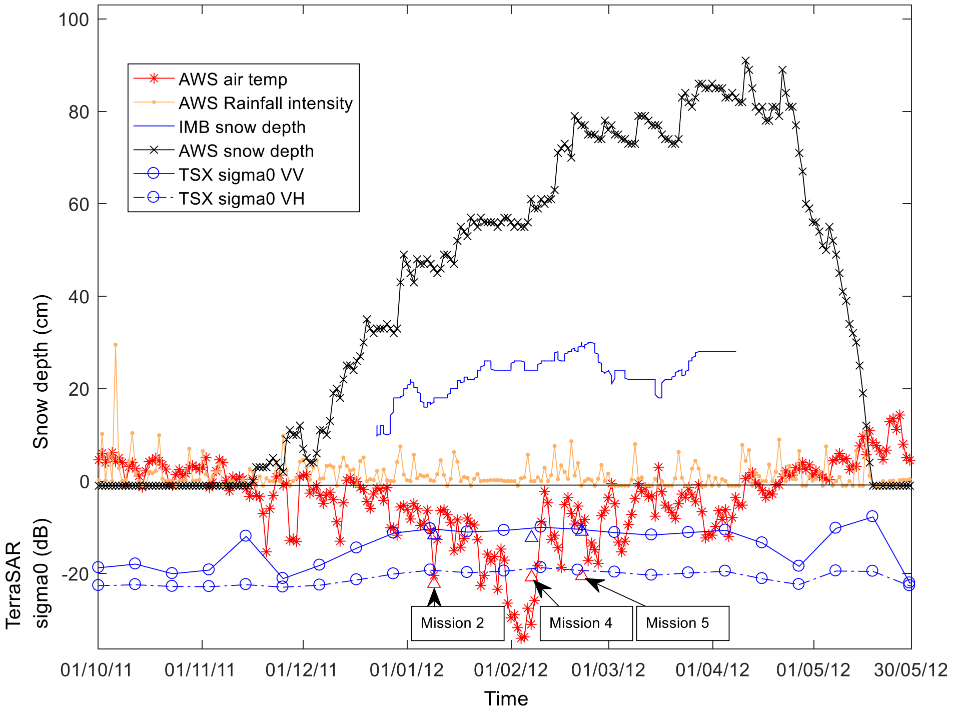

(a)

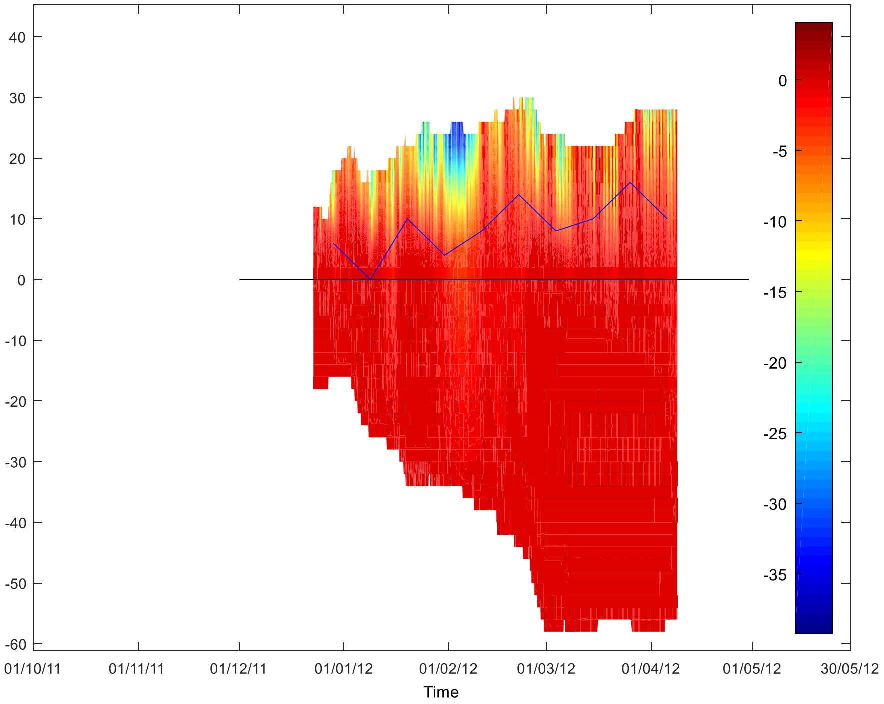

(b)

Figure 9. (a) IMB snow depth data from the IMB measurement location in the Lake Orajärvi for 2011-2012. In addition, the mean TSX σ° at IMB location for both VV and VH polarisations, AWS snow depth [cm], air temperature [°C], and rainfall intensity [mm] as well as SnowSAR data for the missions 2, 4 and 5 as blue and red triangles for VV and VH polarization, respectively, are shown. (b) Time

series of the temperature fields inside the snow and ice from the IMB data. The layer with the temperature between -1.75 °C and -2.5 °C at 18:00 LT on the days of the TSX image acquisition is shown separately as a blue curve in the temperature field.

4. Discussion

Backscattering from snow covered lake or sea ice is a complex function of various snow and ice parameters (e.g. snow depth and snow grain size), and is composed of various surface and volume scattering components, whose relative magnitudes depend on the snow and ice properties. These complexities add challenge to deriving relations between measured σ^0 and bulk snow properties such as snow depth or SWE, which would be needed to enhance the accuracy of present lake and sea ice mass balance estimates. However, as sufficient information on ice and snow structural properties is typically unavailable at the accuracy required to properly set up retrieval algorithms based on complex simulation schemes (see e.g. [45]), analyzing direct relations of σ^0 and bulk snow properties remain appealing as such analysis gives indications of the usability of the SAR data for practical operational retrieval schemes.

For lake ice, we showed that the X-band VH-polarized σ^0 and the Ku-band VV/VH- or KuVH/XVH ratio exhibited the highest direct sensitivity to the snow depth; however, statistically significant relations appeared only for one of the investigated missions with co-incident SAR and in situ information available. For sea ice, the highest sensitivity to the snow depth was found from the Ku-band VV-polarised σ^0 and the Ku-band VV/VH-ratio. However, in the linear regression analysis the observed coefficients of determination were found to be weak or moderate, indicating that snow depth alone was insufficient to explain the observed patterns in the σ^0 data, and other factors such as variations in ice surface roughness, ice and air inclusions, and snow microstructure carry a large effect on σ^0 at both X and Ku bands. This is in line with similar studies using the SnowSAR data over land [66], where the overall influence of the bulk snow properties (SWE and snow depth) on σ^0 was found to be largely masked by variations in the snow effective microstructure and ground surface roughness. The observed weak relations indicate that in practice, the relative benefit of the X- and Ku-band SAR in deriving information on the bulk snow properties over ice is limited. However, in particular for the case of the sea ice site here, the range in snow depth was small; more significant snow depth variations could reveal stronger relations in σ^0. In addition, T_a during the SnowSAR acquisition over the sea ice site might have been too warm (moisture in snow) and caused attenuation to the received backscattering signal, although during the in-situ measurements, the snow was qualitatively observed to be dry.

Qualitative analysis of the TSX imagery time series over the Lake Orajärvi covering a whole winter period gave indications of the complexity of factors affecting σ^0 for snow covered lake ice. Metamorphism processes in both the snow and underlying ice due to weather effects and physical stresses result in a highly variable temporal σ^0 response. However, our results confirm X-band SAR to be a useful tool in monitoring events such as onset and breakup of ice, slushing events on the ice surface, wetting of the ice/snow during the spring. Previous studies of lake ice phenology have mostly used C-band SAR and QuickSAT Ku-band scatterometer data and focused on the Arctic regions [52]. Together with ice type classification based on C-band SAR observations (e.g. [67]), X-band SAR observations may find further operational use in ice charting of freshwater lakes, with implications on ice safety management.

The main reason for the better result for the mission 4 than other missions could be the scale of snow depths in the dataset, that the standard deviation of ice thickness was smaller than in the mission 2, suggesting that the ice could have been more like level ice. The ice was thicker in the mission 4 than in the mission 2, and before SnowSAR data acquisition in the mission 4 there had been cold air temperatures and it was snowing fresh snow just before the SnowSAR data acquisition.

The presented analysis was limited to a single lake and sea ice campaign; the work should be continued by investigating more comprehensive datasets representing diverse sea and lake ice conditions; more comprehensive measurements of variables such as ice surface roughness, air bubble inclusions in ice, snow density, temperature, grain size, SWE, and moisture would be required in order to make more reliable conclusions of the behavior of the σ^o vs. snow depth on ice. In the future, it would be interesting to investigate the capability to estimate the snow depth from the SAR data with combinations of other frequencies such as Ka-band, as well as for different ice types. In addition, theoretical σ^o models, and possibly polarimetric X- and Ku-band SAR data could be used to reveal radar signal characteristics and relations to snow properties which were not analysed here.

5. Conclusions

We investigated the relationship between σ^o measured using an airborne SAR instrument (SnowSAR) operating at the X- and Ku-bands, and the snow depth measured in-situ, over lake ice in the Lake Orajärvi in the northern Finland and sea ice in the Bay of Bothnia of the Baltic Sea. To our knowledge, this study is the first comprehensive survey of airborne SAR σ^o signatures at the X- and Ku-bands over both lake and sea ice. Airborne SAR surveys at these frequencies are necessary to increase our understanding of the complex radar signatures of snow-covered ice. Specifically, this study is one of the first ones analyzing spatially distributed signatures at the Ku-band, which due to the short wavelength, is sensitive to properties of dry snow pack through volume scattering [45].

For lake ice, for the mission 4, we showed that the best correlations between the σ^o and snow depth were found for the X-band VH-polarized σ^o and σ^o polarization ratio of KuVV/KuVH or KuVH/XVH. A statistically significant increase in backscatter with increasing snow depth was found for all individual channels; however, the calculated coefficient of determination for the linear regression was weak or moderate (0.2-0.4). However, these relations seem incidental, as they appeared for only one of the investigated SnowSAR missions. For several subsequent and preceding missions, statistically significant relations between backscatter and snow depth could not be identified. For some cases, the number of data samples was limited, and the distribution in snow depth too small to provide a reliable analysis. However, the major reason for the loss of sensitivity may be due to changes in the subnivean ice backscattering conditions, which change notably both spatially and temporally, and possibly supersede any variability induced by variations in volume scattering from snow depth. This is supported by analysis of the TerraSAR-X data over the same lake, which shows notable spatio-temporal variability of the X-band backscattering signal, which qualitatively can be attributed to e.g. cracks and slushing of water on the ice-snow interface, causing visible variations in backscattering conditions.

For sea ice, the small amount of coincident SnowSAR and in-situ data limited the reliability of analyzed relationships between the SnowSAR σ^o and the in-situ snow depth. However, based on the limited data, the Ku-band VV-polarization σ^o and the polarization ratio KuVV/KuVH showed the highest sensitivity to the snow depth. As for lake ice, the Ku-band σ^o increased with the increasing snow depth, indicating an increase of snow volume scattering. However, the X-band signatures over sea ice revealed less sensitivity than over lake ice. Overall, the observed relations were weaker than for lake ice (max R2 was 0.21). The different results for lake and sea ice are possibly due to different dataset sizes, different ranges in snow depth or differences in stratigraphy and properties in snow cover over lake and sea ice, and differences in ice surface roughness and ice medium properties (e.g. fresh lake ice vs. slightly saline sea ice).

TSX SAR data was used along with the Ice Mass Balance Buoy (IMB) data from the Lake Orajärvi to compare the evolution of snow depth and σ^o. As expected, seasonal variation of the snow depth on lake ice was observed. The analysis of the TSX σ^o timeseries gives indications of the complexity of factors affecting backscattering over snow covered ice. However, X-band SAR can be a useful tool to monitor for example the onset and breakup of ice, slushing events on the ice surface or wetting of the ice/snow in spring.

In general, the results indicate that obtaining reliable estimates of snow depth over lake and sea ice would be challenging by using only X and Ku band backscattering information.

Author Contributions: Software, K.V. and J.C.; formal analysis, K.V.; data curation, K.V. and J.C.; writing—original draft preparation, K.V.; writing—review and editing, J.C., M.M., J.L, J.P. and B.C.; supervision, J.L.; project administration, J.L.; funding acquisition; J.L. All authors have read and agreed to the published version of the manuscript.

Acknowledgments: This study was a part of ESA's SILIRIS (Sea Ice, Lake Ice and River Ice Study) -study focused on development of sea ice and lake and river ice retrieval algorithms for CoReH2O. We thank ESA for providing the SnowSAR data and all the teams involved in in-situ measurements. The German Aerospace Agency (DLR) is acknowledged for providing the TerraSAR-X imagery.

Conflicts of Interest: The authors declare no conflict of interest. The founding sponsors had no role in the design of the study; in the collection, analyses, or interpretation of data; in the writing of the manuscript, and in the decision to publish the results.

Appendix A

Here the results for the missions 2 and 5 are presented in detail. In Table A1 and Table A2, the statistics of the linear regression between the SnowSAR σ⁰ data and the in-situ snow depth are shown (see Table 3 for the mission 4). In Figure A1 and Figure A2 scatterplots between the snow depth and the mean σ⁰ at the four SnowSAR channels and the four channel ratios are shown for the missions 2 and 5. In addition, Figure A4 shows data from all the three missions together. The ins-situ sampling tracks for the missions 2, 4 and 5 on the SnowSAR mosaics are shown in Figure A3.

Table A1. The statistics of the linear regression between the SnowSAR backscattering coefficient data and the in-situ snow depth for the mission 2 in the lake ice site.

Lake				
	SLOPE TERM [DB/CM]	AVERAGE [DB]	R2	P-VALUE
XVV	0.00	-11.7	0.00	0.795
XVH	-0.00	-22.2	0.00	0.864
KuVV	-0.02	-9.2	0.00	0.438
KuVH	-0.02	-16.4	0.00	0.584
KuVV/KuVH	0.00	7.4	0.00	0.886
XVV/XVH	0.01	10.6	0.00	0.417
KuVV/XVV	-0.03	2.4	**0.02**	0.052
KuVH/XVH	-0.02	5.7	0.01	0.233

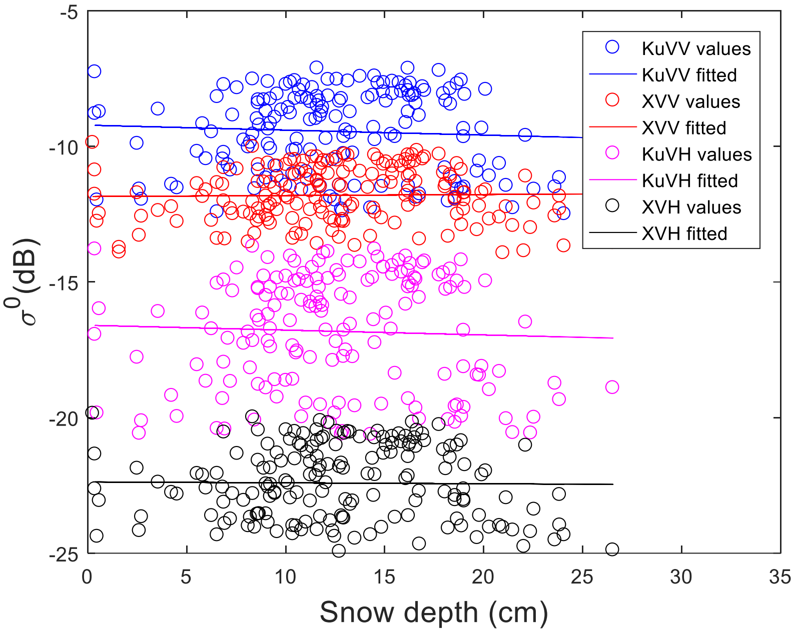

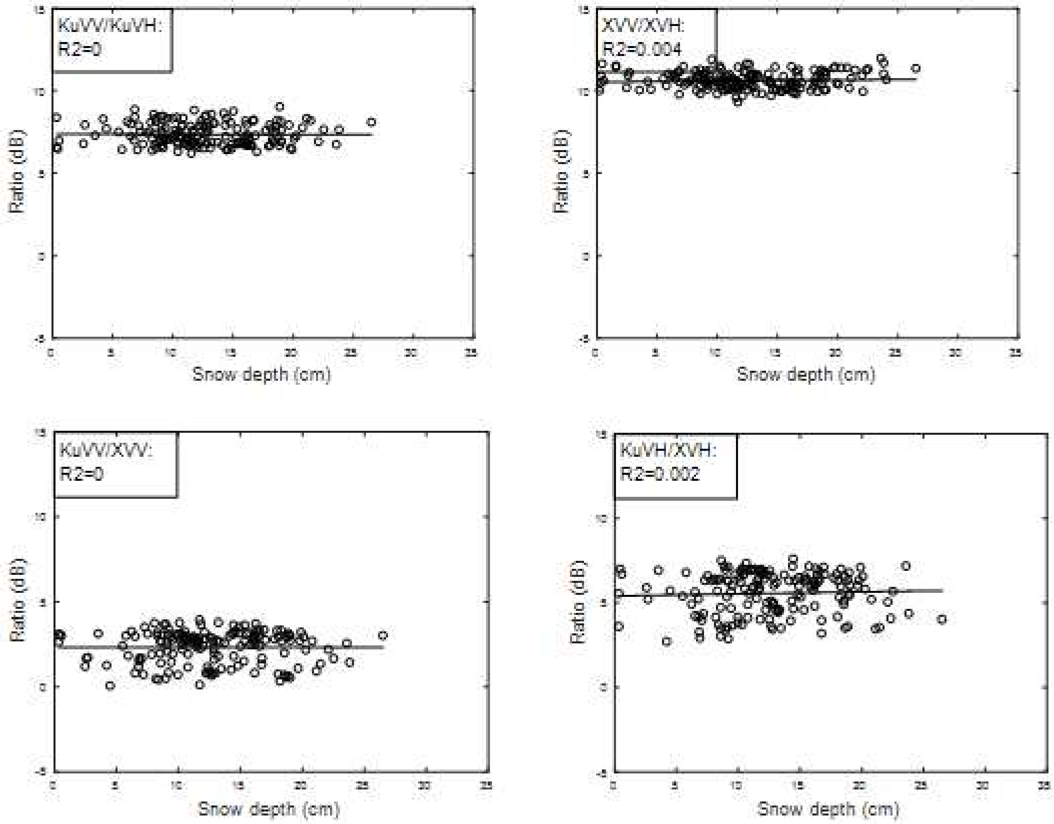

Figure A1. SnowSAR X- and Ku-band backscattering coefficients and their ratios as a function of snow depth on the Lake Orajärvi for the mission 2. The σ^o was scaled to the reference incidence angle of 43.8 deg for the Ku-band and 43 deg for the X-band.

Table A2. The statistics of the linear regression between the SnowSAR backscattering coefficient data and the in-situ snow depth for the mission 5 in the lake ice site.

Lake				
	SLOPE TERM [DB/CM]	AVERAGE [DB]	R2	P-VALUE
XVV	0.00	-10.9	0.00	0.845
XVH	-0.02	-20.5	0.00	0.060
KuVV	-0.01	-8.8	0.00	0.400
KuVH	0.03	-16.6	**0.02**	< 0.001
KuVV/KuVH	-0.01	7.9	0.01	0.005
XVV/XVH	0.02	9.7	**0.02**	< 0.001
KuVV/XVV	-0.01	2.1	0.01	0.033
KuVH/XVH	0.02	3.9	0.02	< 0.001

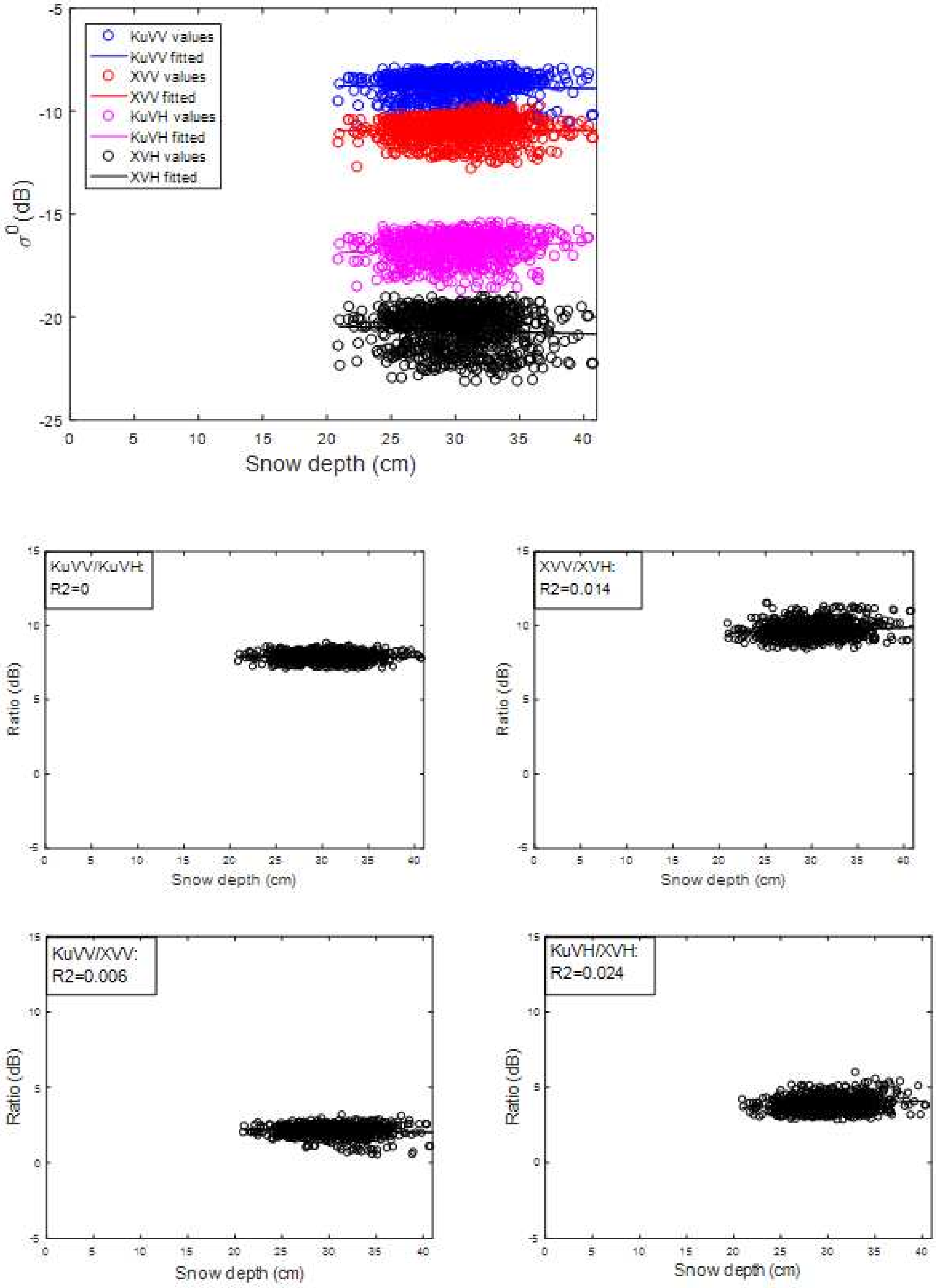

Figure A2. SnowSAR X- and Ku-band backscattering coefficients and their ratios as a function of snow depth on the Lake Orajärvi for the mission 5. The σ^0 was scaled to the reference incidence angle of 43.8 deg for the Ku-band and 43 deg for the X-band.

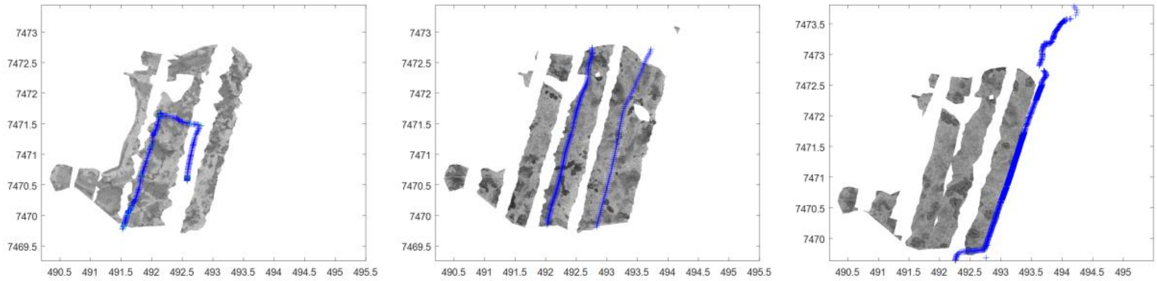

Figure A3. SnowSAR and in situ data (in blue) used for the mission 2 (on the left), mission 4 (in the middle) and mission 5 (on the right) shown on Lake Orajärvi.

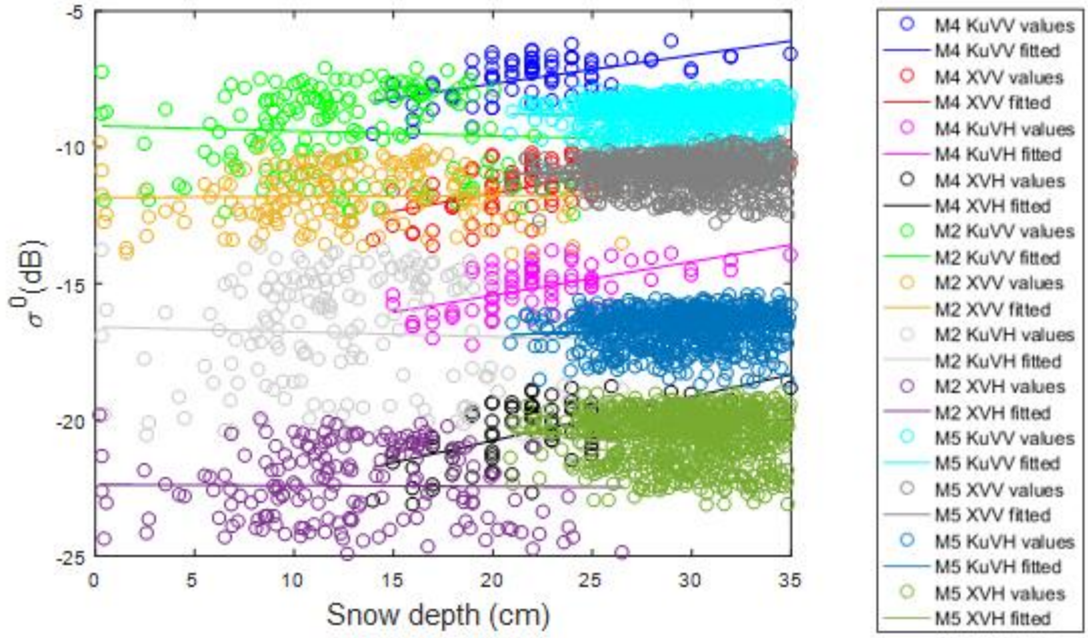

Figure A4. Mission 2 (on the left), mission 4 (in the middle) and mission 5 (on the right) in the same image.

References

1. Maykut, G.A. Energy Exchange over Young Sea Ice in the Central Arctic. *J. Geophys. Res. Oceans* **1978**, *83*, 3646–3658, doi:10.1029/JC083iC07p03646.
2. Leppäranta, M. A Growth Model for Black Ice, Snow Ice and Snow Thickness in Subarctic Basins. *Hydrol. Res.* **1983**, *14*, 59–70, doi:10.2166/nh.1983.0006.
3. Fichefet, T.; Maqueda, M.A.M. Modelling the Influence of Snow Accumulation and Snow-Ice Formation on the Seasonal Cycle of the Antarctic Sea-Ice Cover. *Clim. Dyn.* **1999**, *15*, 251–268, doi:10.1007/s003820050280.
4. Giles, K.A.; Laxon, S.W.; Wingham, D.J.; Wallis, D.W.; Krabill, W.B.; Leuschen, C.J.; McAdoo, D.; Manizade, S.S.; Raney, R.K. Combined Airborne Laser and Radar Altimeter Measurements over the Fram Strait in May 2002. *Remote Sens. Environ.* **2007**, *111*, 182–194, doi:10.1016/j.rse.2007.02.037.
5. Shen, X.; Ke, C.-Q.; Wang, Q.; Zhang, J.; Shi, L.; Zhang, X. Assessment of Arctic Sea Ice Thickness Estimates From ICESat-2 Using IceBird Airborne Measurements. *IEEE Trans. Geosci. Remote Sens.* **2021**, *59*, 3764–3775, doi:10.1109/TGRS.2020.3022945.
6. Kurtz, N.T.; Farrell, S.L. Large-Scale Surveys of Snow Depth on Arctic Sea Ice from Operation IceBridge. *Geophys. Res. Lett.* **2011**, *38*, n/a-n/a, doi:10.1029/2011GL049216.
7. Brucker, L.; Markus, T. Arctic-Scale Assessment of Satellite Passive Microwave-Derived Snow Depth on Sea Ice Using Operation IceBridge Airborne Data. *J. Geophys. Res. Oceans* **2013**, *118*, 2892–2905, doi:10.1002/jgrc.20228.

8. Yan, J.-B.; Gomez-Garcia Alvestegui, D.; McDaniel, J.W.; Li, Y.; Gogineni, S.; Rodriguez-Morales, F.; Brozena, J.; Leuschen, C.J. Ultrawideband FMCW Radar for Airborne Measurements of Snow Over Sea Ice and Land. *IEEE Trans. Geosci. Remote Sens.* **2017**, *55*, 834–843, doi:10.1109/TGRS.2016.2616134.
9. Rodriguez-Morales, F.; Leuschen, C.; Carabajal, C.L.; Paden, J.; Wolf, J.A.; Garrison, S.; McDaniel, J.W. An Improved UWB Microwave Radar for Very Long-Range Measurements of Snow Cover. *IEEE Trans. Instrum. Meas.* **2020**, *69*, 7761–7772, doi:10.1109/TIM.2020.2982813.
10. Jenssen, R.O.R.; Eckerstorfer, M.; Jacobsen, S. Drone-Mounted Ultrawideband Radar for Retrieval of Snowpack Properties. *IEEE Trans. Instrum. Meas.* **2020**, *69*, 221–230, doi:10.1109/TIM.2019.2893043.
11. Murfitt, J.; Duguay, C.R. 50 Years of Lake Ice Research from Active Microwave Remote Sensing: Progress and Prospects. *Remote Sens. Environ.* **2021**, *264*, 112616, doi:10.1016/j.rse.2021.112616.
12. Markus, T.; Cavalieri, D.J. Snow Depth Distribution Over Sea Ice in the Southern Ocean from Satellite Passive Microwave Data. In *Antarctic Research Series*; Jeffries, M.O., Ed.; American Geophysical Union: Washington, D. C., 2013; pp. 19–39 ISBN 978-1-118-66824-5.
13. Hallikainen, M.; Winebrenner, D.P. The Physical Basis for Sea Ice Remote Sensing. In *Geophysical Monograph Series*; Carsey, F.D., Ed.; American Geophysical Union: Washington, D. C., 1992; Vol. 68, pp. 29–46 ISBN 978-0-87590-033-9.
14. Du, J.; Kimball, J.S.; Duguay, C.; Kim, Y.; Watts, J.D. Satellite Microwave Assessment of Northern Hemisphere Lake Ice Phenology from 2002 to 2015. *The Cryosphere* **2017**, *11*, 47–63, doi:10.5194/tc-11-47-2017.
15. Rott, H.; Yueh, S.H.; Cline, D.W.; Duguay, C.; Essery, R.; Haas, C.; Hélière, F.; Kern, M.; Macelloni, G.; Malnes, E.; et al. Cold Regions Hydrology High-Resolution Observatory for Snow and Cold Land Processes. *Proc. IEEE* **2010**, *98*, 752–765, doi:10.1109/JPROC.2009.2038947.
16. Comiso, J.C.; Cavalieri, D.J.; Markus, T. Sea Ice Concentration, Ice Temperature, and Snow Depth Using AMSR-E Data. *IEEE Trans. Geosci. Remote Sens.* **2003**, *41*, 243–252, doi:10.1109/TGRS.2002.808317.
17. Maaß, N.; Kaleschke, L.; Tian-Kunze, X.; Drusch, M. Snow Thickness Retrieval over Thick Arctic Sea Ice Using SMOS Satellite Data. *The Cryosphere* **2013**, *7*, 1971–1989, doi:10.5194/tc-7-1971-2013.
18. Markus, T.; Cavalieri, D.J.; Gasiewski, A.J.; Klein, M.; Maslanik, J.A.; Powell, D.C.; Stankov, B.B.; Stroeve, J.C.; Sturm, M. Microwave Signatures of Snow on Sea Ice: Observations. *IEEE Trans. Geosci. Remote Sens.* **2006**, *44*, 3081–3090, doi:10.1109/TGRS.2006.883134.
19. Kern, S.; Ozsoy-Cicek, B.; Willmes, S.; Nicolaus, M.; Haas, C.; Ackley, S. An Intercomparison between AMSR-E Snow-Depth and Satellite C- and Ku-Band Radar Backscatter Data for Antarctic Sea Ice. *Ann. Glaciol.* **2011**, *52*, 279–290, doi:10.3189/172756411795931750.
20. Merkouriadi, I.; Cheng, B.; Graham, R.M.; Rösel, A.; Granskog, M.A. Critical Role of Snow on Sea Ice Growth in the Atlantic Sector of the Arctic Ocean. *Geophys. Res. Lett.* **2017**, *44*, 10,479-10,485, doi:10.1002/2017GL075494.
21. Cheng, B.; Zhang, Z.; Vihma, T.; Johansson, M.; Bian, L.; Li, Z.; Wu, H. Model Experiments on Snow and Ice Thermodynamics in the Arctic Ocean with CHINARE 2003 Data. *J. Geophys. Res.* **2008**, *113*, C09020, doi:10.1029/2007JC004654.
22. Kern, S.; Ozsoy-Çiçek, B. Satellite Remote Sensing of Snow Depth on Antarctic Sea Ice: An Inter-Comparison of Two Empirical Approaches. *Remote Sens.* **2016**, *8*, 450, doi:10.3390/rs8060450.
23. Lawrence, I.R.; Tsamados, M.C.; Stroeve, J.C.; Armitage, T.W.K.; Ridout, A.L. Estimating Snow Depth over Arctic Sea Ice from Calibrated Dual-Frequency Radar Freeboards. *The Cryosphere* **2018**, *12*, 3551–3564, doi:10.5194/tc-12-3551-2018.
24. Kwok, R.; Kacimi, S.; Webster, M.A.; Kurtz, N.T.; Petty, A.A. Arctic Snow Depth and Sea Ice Thickness From ICESat-2 and CryoSat-2 Freeboards: A First Examination. *J. Geophys. Res. Oceans* **2020**, *125*, doi:10.1029/2019JC016008.
25. Kern, M.; Cullen, R.; Berruti, B.; Bouffard, J.; Casal, T.; Drinkwater, M.R.; Gabriele, A.; Lecuyot, A.; Ludwig, M.; Midthassel, R.; et al. The Copernicus Polar Ice and Snow Topography Altimeter (CRISTAL) High-Priority Candidate Mission. *The Cryosphere* **2020**, *14*, 2235–2251, doi:10.5194/tc-14-2235-2020.
26. Wei, L.; Deng, X.; Cheng, B.; Vihma, T.; Hannula, H.-R.; Qin, T.; Pulliainen, J. The Impact of Meteorological Conditions on Snow and Ice Thickness in an Arctic Lake. *Tellus Dyn. Meteorol. Oceanogr.* **2016**, *68*, 31590, doi:10.3402/tellusa.v68.31590.
27. Cheng, B.; Vihma, T.; Rontu, L.; Kontu, A.; Pour, H.K.; Duguay, C.; Pulliainen, J. Evolution of Snow and Ice Temperature, Thickness and Energy Balance in Lake Orajärvi, Northern Finland. *Tellus Dyn. Meteorol. Oceanogr.* **2014**, *66*, 21564, doi:10.3402/tellusa.v66.21564.
28. Murfitt, J.; Duguay, C.R.; Picard, G.; Gunn, G.E. Investigating the Effect of Lake Ice Properties on Multifrequency Backscatter Using the Snow Microwave Radiative Transfer Model. *IEEE Trans. Geosci. Remote Sens.* **2022**, *60*, 1–23, doi:10.1109/TGRS.2022.3197109.
29. Beckers, J.F.; Alec Casey, J.; Haas, C. Retrievals of Lake Ice Thickness From Great Slave Lake and Great Bear Lake Using CryoSat-2. *IEEE Trans. Geosci. Remote Sens.* **2017**, *55*, 3708–3720, doi:10.1109/TGRS.2017.2677583.

30. Kheyrollah Pour, H.; Duguay, C.R.; Scott, K.A.; Kang, K.-K. Improvement of Lake Ice Thickness Retrieval From MODIS Satellite Data Using a Thermodynamic Model. *IEEE Trans. Geosci. Remote Sens.* **2017**, *55*, 5956–5965, doi:10.1109/TGRS.2017.2718533.
31. Zhou, L.; Stroeve, J.; Xu, S.; Petty, A.; Tilling, R.; Winstrup, M.; Rostosky, P.; Lawrence, I.R.; Liston, G.E.; Ridout, A.; et al. Inter-Comparison of Snow Depth over Arctic Sea Ice from Reanalysis Reconstructions and Satellite Retrieval. *The Cryosphere* **2021**, *15*, 345–367, doi:10.5194/tc-15-345-2021.
32. Yackel, J.J.; Barber, D.G. Observations of Snow Water Equivalent Change on Landfast First-Year Sea Ice in Winter Using Synthetic Aperture Radar Data. *IEEE Trans. Geosci. Remote Sens.* **2007**, *45*, 1005–1015, doi:10.1109/TGRS.2006.890418.
33. Paul, S.; Willmes, S.; Hoppmann, M.; Hunkeler, P.A.; Wesche, C.; Nicolaus, M.; Heinemann, G.; Timmermann, R. The Impact of Early-Summer Snow Properties on Antarctic Landfast Sea-Ice X-Band Backscatter. *Ann. Glaciol.* **2015**, *56*, 263–273, doi:10.3189/2015AoG69A715.
34. Gill, J.P.S.; Yackel, J.J.; Geldsetzer, T.; Fuller, M.C. Sensitivity of C-Band Synthetic Aperture Radar Polarimetric Parameters to Snow Thickness over Landfast Smooth First-Year Sea Ice. *Remote Sens. Environ.* **2015**, *166*, 34–49, doi:10.1016/j.rse.2015.06.005.
35. Young-Soo Kim; Onstott, R.; Moore, R. Effect of a Snow Cover on Microwave Backscatter from Sea Ice. *IEEE J. Ocean. Eng.* **1984**, *9*, 383–388, doi:10.1109/JOE.1984.1145649.
36. Nghiem, S.V.; Wu-Yang Tsai Global Snow Cover Monitoring with Spaceborne K/Sub u/-Band Scatterometer. *IEEE Trans. Geosci. Remote Sens.* **2001**, *39*, 2118–2134, doi:10.1109/36.957275.
37. Eriksson, L.E.B.; Borenäs, K.; Dierking, W.; Berg, A.; Santoro, M.; Pemberton, P.; Lindh, H.; Karlson, B. Evaluation of New Spaceborne SAR Sensors for Sea-Ice Monitoring in the Baltic Sea. *Can. J. Remote Sens.* **2010**, *36*, S56–S73, doi:10.5589/m10-020.
38. Nandan, V.; Geldsetzer, T.; Islam, T.; Yackel, John.J.; Gill, J.P.S.; Fuller, Mark.C.; Gunn, G.; Duguay, C. Ku-, X- and C-Band Measured and Modeled Microwave Backscatter from a Highly Saline Snow Cover on First-Year Sea Ice. *Remote Sens. Environ.* **2016**, *187*, 62–75, doi:10.1016/j.rse.2016.10.004.
39. Ulaby, F.T.; Moore, R.K.; Fung, A.K. *Microwave Remote Sensing. 2: Radar Remote Sensing and Surface Scattering and Emission Theory*; Remote sensing; Addison-Wesley: Reading, Mass, 1982; ISBN 978-0-201-10760-9.
40. Fung, A.K. *Microwave Scattering and Emission Models and Their Applications*; The Artech House remote sensing library; Artech House: Boston, 1994; ISBN 978-0-89006-523-5.
41. Barber, D.G.; Fung, A.K.; Grenfell, T.C.; Nghiem, S.V.; Onstott, R.G.; Lytle, V.I.; Perovich, D.K.; Gow, A.J. The Role of Snow on Microwave Emission and Scattering over First-Year Sea Ice. *IEEE Trans. Geosci. Remote Sens.* **1998**, *36*, 1750–1763, doi:10.1109/36.718643.
42. Shokr, M.; Dabboor, M. Observations of SAR Polarimetric Parameters of Lake and Fast Sea Ice during the Early Growth Phase. *Remote Sens. Environ.* **2020**, *247*, 111910, doi:10.1016/j.rse.2020.111910.
43. Shaposhnikova, M.; Duguay, C.; Roy-Léveillée, P. Bedfast and Floating-Ice Dynamics of Thermokarst Lakes Using a Temporal Deep-Learning Mapping Approach: Case Study of the Old Crow Flats, Yukon, Canada. *The Cryosphere* **2023**, *17*, 1697–1721, doi:10.5194/tc-17-1697-2023.
44. Gunn, G.E.; Duguay, C.R.; Atwood, D.K.; King, J.; Toose, P. Observing Scattering Mechanisms of Bubbled Freshwater Lake Ice Using Polarimetric RADARSAT-2 (C-Band) and UW-Scat (X- and Ku-Bands). *IEEE Trans. Geosci. Remote Sens.* **2018**, *56*, 2887–2903, doi:10.1109/TGRS.2017.2786158.
45. Gunn, G.E.; Brogioni, M.; Duguay, C.; Macelloni, G.; Kasurak, A.; King, J. Observation and Modeling of X- and Ku-Band Backscatter of Snow-Covered Freshwater Lake Ice. *IEEE J. Sel. Top. Appl. Earth Obs. Remote Sens.* **2015**, *8*, 3629–3642, doi:10.1109/JSTARS.2015.2420411.
46. Gunn, G.E.; Duguay, C.R.; Brown, L.C.; King, J.; Atwood, D.; Kasurak, A. Freshwater Lake Ice Thickness Derived Using Surface-Based X- and Ku-Band FMCW Scatterometers. *Cold Reg. Sci. Technol.* **2015**, *120*, 115–126, doi:10.1016/j.coldregions.2015.09.012.
47. Nghiem, S.V.; Leshkevich, G.A. Satellite SAR Remote Sensing of Great Lakes Ice Cover, Part 1. Ice Backscatter Signatures at C Band. *J. Gt. Lakes Res.* **2007**, *33*, 722–735, doi:10.3394/0380-1330(2007)33[722:SSRSOG]2.0.CO;2.
48. Geldsetzer, T.; Sanden, J. van der; Brisco, B. Monitoring Lake Ice during Spring Melt Using RADARSAT-2 SAR. *Can. J. Remote Sens.* **2010**, *36*, S391–S400, doi:10.5589/m11-001.
49. Sobiech, J.; Dierking, W. Observing Lake- and River-Ice Decay with SAR: Advantages and Limitations of the Unsupervised *k* -Means Classification Approach. *Ann. Glaciol.* **2013**, *54*, 65–72, doi:10.3189/2013AoG62A037.
50. Engram, M.; Arp, C.D.; Jones, B.M.; Ajadi, O.A.; Meyer, F.J. Analyzing Floating and Bedfast Lake Ice Regimes across Arctic Alaska Using 25 Years of Space-Borne SAR Imagery. *Remote Sens. Environ.* **2018**, *209*, 660–676, doi:10.1016/j.rse.2018.02.022.
51. Ferguson, J.E.; Gunn, G.E. Polarimetric Decomposition of Microwave-Band Freshwater Ice SAR Data: Review, Analysis, and Future Directions. *Remote Sens. Environ.* **2022**, *280*, 113176, doi:10.1016/j.rse.2022.113176.

52. Duguay, C.R.; Bernier, M.; Gauthier, Y.; Kouraev, A. Remote Sensing of Lake and River Ice. In *Remote Sensing of the Cryosphere*; Tedesco, M., Ed.; John Wiley & Sons, Ltd: Chichester, UK, 2014; pp. 273–306 ISBN 978-1-118-36890-9.
53. Trampuz, C.; et al. *Technical Assistance for the Development and Deployment of an X- and Ku- Band MiniSAR Airborne System*; 2011;
54. Palosuo, E.; Leppäranta, M.; Seinä, A. *Formation,_thickness_and_stability_of_fast_ice_along_the_Finnish_coast*; Winter Navig. Res. Board; Helsinki, Finland, 1982;
55. Hallikainen, M. Microwave Remote Sensing of Low-Salinity Sea Ice. In *Geophysical Monograph Series*; Carsey, F.D., Ed.; American Geophysical Union: Washington, D. C., 1992; Vol. 68, pp. 361–373 ISBN 978-0-87590-033-9.
56. Di Leo, D.; Coccia, A.; Meta, A. Technical Assistance for the Development and Deployment of an X- and Ku-Band MiniSAR Airborne System (SnowSAR) 2015.
57. Schwerdt, M.; Schmidt, K.; Klenk, P.; Tous Ramon, N.; Rudolf, D.; Raab, S.; Weidenhaupt, K.; Reimann, J.; Zink, M. Radiometric Performance of the TerraSAR-X Mission over More Than Ten Years of Operation. *Remote Sens.* **2018**, *10*, 754, doi:10.3390/rs10050754.
58. Lemmetyinen, J.; Kontu, A.; Pulliainen, J.; Mäkynen, M. *Synergy of CoReH2O SAR and Microwave Radiometry Data to Retrieve Snow and Ice Parameters.*; 2013;
59. Makynen, M.; Bin Cheng; Simila, M.; Vihma, T.; Hallikainen, M. Interpretation of C-Band SAR Backscattering Coefficient Time Series for the Baltic Sea Landfast Sea Ice Using a 1-D Thermodynamic Snow/Ice Model. In Proceedings of the 2007 IEEE International Geoscience and Remote Sensing Symposium; IEEE: Barcelona, Spain, 2007; pp. 3983–3986.
60. Paterson, W.S.B. *The Physics of Glaciers*; 3rd ed.; Pergamon: Oxford, OX, England ; Tarrytown, N.Y., U.S.A, 1994; ISBN 978-0-08-037945-6.
61. Kontu, A. *Effect of Snow Microstructure and Subnivean Water Bodies on Microwave Radiometry of Seasonal Snow*; 2018; ISBN 978-952-336-051-8.
62. Howell, S.E.L.; Brown, L.C.; Kang, K.-K.; Duguay, C.R. Variability in Ice Phenology on Great Bear Lake and Great Slave Lake, Northwest Territories, Canada, from SeaWinds/QuikSCAT: 2000–2006. *Remote Sens. Environ.* **2009**, *113*, 816–834, doi:10.1016/j.rse.2008.12.007.
63. Shokr, M., Sinha, N. *Sea Ice: Physics and Remote Sensing*; 2015; ISBN 978-1-119-02789-8.
64. Leinss, S.; Parrella, G.; Hajnsek, I. Snow Height Determination by Polarimetric Phase Differences in X-Band SAR Data. *IEEE J. Sel. Top. Appl. Earth Obs. Remote Sens.* **2014**, *7*, 3794–3810, doi:10.1109/JSTARS.2014.2323199.
65. Cai, Y.; Ke, C.-Q.; Duan, Z. Monitoring Ice Variations in Qinghai Lake from 1979 to 2016 Using Passive Microwave Remote Sensing Data. *Sci. Total Environ.* **2017**, *607–608*, 120–131, doi:10.1016/j.scitotenv.2017.07.027.
66. King, J.; Derksen, C.; Toose, P.; Langlois, A.; Larsen, C.; Lemmetyinen, J.; Marsh, P.; Montpetit, B.; Roy, A.; Rutter, N.; et al. The Influence of Snow Microstructure on Dual-Frequency Radar Measurements in a Tundra Environment. *Remote Sens. Environ.* **2018**, *215*, 242–254, doi:10.1016/j.rse.2018.05.028.
67. Leshkevich, G.; Nghiem, S.V. Great Lakes Ice Classification Using Satellite C-Band SAR Multi-Polarization Data. *J. Gt. Lakes Res.* **2013**, *39*, 55–64, doi:10.1016/j.jglr.2013.05.003.